$\pi^- p \to \eta^{(\prime)} \pi^- p$ in the double Regge region

Ł. Bibrzycki,[1,2,3,*] C. Fernández-Ramírez,[4,†] V. Mathieu,[5,6] M. Mikhasenko,[7]
M. Albaladejo,[3] A. N. Hiller Blin,[3] A. Pilloni,[8] and A. P. Szczepaniak[2,3,9]
(Joint Physics Analysis Center)

[1] *Pedagogical University of Krakow, 30-084 Kraków, Poland*
[2] *Department of Physics, Indiana University, Bloomington, IN 47405, USA*
[3] *Theory Center, Thomas Jefferson National Accelerator Facility, Newport News, VA 23606, USA*
[4] *Instituto de Ciencias Nucleares, Universidad Nacional Autónoma de México, Ciudad de México 04510, Mexico*
[5] *Departament de Física Quàntica i Astrofísica and Institut de Ciències del Cosmos, Universitat de Barcelona, Martí i Franquès 1, E08028, Spain*
[6] *Departamento de Física Teórica, Universidad Complutense de Madrid and IPARCOS, 28040 Madrid, Spain*
[7] *CERN, 1211 Geneva 23, Switzerland*
[8] *INFN Sezione di Roma, Roma, I-00185, Italy*
[9] *Center for Exploration of Energy and Matter, Indiana University, Bloomington, IN 47403, USA*

(Dated: April 20, 2021)

The production of $\eta^{(\prime)}\pi$ pairs constitutes one of the golden channels to search for hybrid exotics, with explicit gluonic degrees of freedom. Understanding the dynamics and backgrounds associated to $\eta^{(\prime)}\pi$ production above the resonance region is required to impose additional constraints to the resonance extraction. We consider the reaction $\pi^- p \to \pi^- \eta^{(\prime)} p$ measured by COMPASS. We show that the data in $2.4 < m_{\eta^{(\prime)}\pi} < 3.0\,\text{GeV}$ can be described by amplitudes based on double Regge exchanges. The angular distribution of the meson pairs, in particular in the $\eta'\pi$ channel, can be attributed to flavor singlet exchanges, suggesting the presence of a large gluon content that couples strongly to the produced mesons.

I. INTRODUCTION

Since the early days of the quark model, hadron spectroscopy has remained central to our understanding of QCD. High precision data on various reactions that have recently been collected from experiments at CERN, JLab, B- and charm factories have produced tantalizing evidence for the existence of exotic states that do not naturally fit within the quark model classification [1–3], *e.g.* pentaquark and tetraquark candidates [4–6]. The quantum numbers of some exotics are manifestly incompatible with a simple $q\bar{q}$ assignment. For example, states with $J^{PC} = 1^{-+}$ have long been speculated to be hybrids, *i.e.* mesons where gluons play the role of constituents [7, 8]. The paucity of data and the need for a thorough partial wave analysis to disentangle resonance from nonresonant background can be a challenging endeavor. The COMPASS collaboration extracted the $\eta\pi$ and $\eta'\pi$ partial waves as a function of the invariant mass, $m_{\eta^{(\prime)}\pi} < 3.0\,\text{GeV}$ from the measurement of diffractive pion dissociation on a nucleon target at 191 GeV [9]. These odd waves carry exotic quantum numbers, $J^{PC} = 1^{-+}$, 3^{-+},... The key observations are that even waves are similar in both reactions, while the P-wave is significantly larger in $\eta'\pi$. This reflects in a larger forward-backward asymmetry of the $\eta'\pi$. Both channels present peaking structures in the P-waves at seemingly different masses. For a a long time, the two structures were interpreted as two different states, the lighter one coupling mainly to $\eta\pi$ and the heavier one to $\eta'\pi$. However, the coupled-channel analysis in [10] showed that the data is consistent with the existence of a single exotic resonance. These conclusions have been confirmed by a recent independent analysis [11] and are supported by the latest lattice QCD computations [12].

At higher invariant masses, the reaction is expected to be dominated by cross-channel Regge exchanges, which is consistent with the cross section peaking in the forward and backward directions, with the peaks shrinking with increasing $\eta^{(\prime)}\pi$ mass *cf.* Fig. 2 of Ref. [9]. Since a forward-backward asymmetry arises from the interference between even and odd waves, the larger exotic P-wave in $\eta'\pi$ is consistent with the observed larger asymmetry. This connection between resonances and Regge exchanges can be formalized *via* dispersion relations, *e.g.* in the form of finite energy sum rules [13–15]. Such relations can be used to constrain fits in the resonance region which, in combination with forthcoming high precision data from GlueX [16, 17] and COMPASS [18], could lead to a more accurate determination of the exotic meson resonance parameters. A necessary step in this procedure is to fit the high mass region with analytical amplitudes that respect Regge asymptotic behavior. This is the main purpose of this work.

The paper is organized as follows. In Section II we describe the COMPASS partial waves, the procedure to compute the intensity distribution from them, and the main features of said distribution. Section III describes the double-Regge model used to fit the data. In Section IV we discuss the consequences of truncating the partial wave expansion in the analysis of the data and

* lukasz.bibrzycki@up.krakow.pl
† cesar.fernandez@nucleares.unam.mx

how it impacts the comparison to a given model and the extraction of the dynamics. In Section V we discuss what are the relevant contributions to the amplitudes, needed to reproduce the features of the angular and mass dependencies. Section VI describes our fitting strategy, fit results, and comparison to data. Section VII provides the connection between the COMPASS partial waves and the partial waves obtained from the double-Regge model. Finally, in Section VIII we summarize our results. The kinematical description of the $\eta^{(\prime)}\pi$ reactions, statistical analysis, error propagation from the COMPASS partial waves to the intensity distribution, and other details and complementary information are left to the Appendices.

II. COMPASS INTENSITIES

In this section we describe the data on reactions

$$\pi^-(q) + p(p_1) \to \eta^{(\prime)}(k_\eta) + \pi^-(k_\pi) + p(p_2)\,, \qquad (1)$$

analyzed by COMPASS in Ref. [9]. The unpolarized cross sections for both reactions depend on five kinematical variables. These are, for example, the total center of mass energy squared $s = (q + p_1)^2$, the invariant mass of the produced meson pair $m^2 = m^2_{\eta^{(\prime)}\pi} = (k_\pi + k_\eta)^2$, the square of the momentum transfer between the target and the recoil nucleon $t_p = (p_1 - p_2)^2$, and the spherical angle Ω determining the direction of the relative momentum between the two mesons in the rest frame of the pair. The COMPASS experiment operated with a fixed beam momentum of $p_{\text{lab}} = 191\,\text{GeV}$; in the analysis of [9] t_p was integrated in the region $t_p \in [-1.0, -0.1]\,\text{GeV}^2$. Furthermore, since there was no measurement of the initial flux, the normalization of the event distribution is unknown. In the partial wave analysis of [9] the angular dependence of the event distribution, *aka* intensity function, in bins of m, was expanded in terms of angular functions,

$$I(m,\Omega) = \sum_{\epsilon=\pm} \left| \sum_{L,M} f^{\epsilon}_{LM}(m)\Psi^{\epsilon}_{LM}(\Omega) \right|^2 , \qquad (2)$$

given by $\Psi^{\epsilon=+}_{LM}(\Omega) = \sqrt{2}Y^M_L(\theta,0)\sin M\phi$ and $\Psi^{\epsilon=-}_{LM}(\Omega) = \sqrt{2}Y^M_L(\theta,0)\cos M\phi$, which are the real spherical harmonics with ϵ referred to as the reflectivity. The angular variables $\Omega \equiv (\theta,\phi)$ determine the direction of the $\eta^{(\prime)}$ in the Gottfried-Jackson (GJ) frame (see Appendix A for the axes orientation). The complex functions $f^{\epsilon}_{LM}(m)$ are obtained by fitting to the angular distributions for each energy bin m. In the strict sense they are not partial waves, as they do not depend on the initial and final nucleon helicities. However, if a single helicity amplitude happens to dominate the reaction, the f's can approach genuine partial waves. In general however, one should think of the f's as defining an effective parametrization of the data at the amplitude level. Nevertheless, in the following we refer to the f's as partial waves, as customary.

In practice, partial wave extraction requires the sum in Eq. (2) to be truncated. In the COMPASS analysis of $\eta\pi$, seven partial waves were used, $(L = 1,\ldots,6; M = 1)$ and $(L = 2; M = 2)$, while for the $\eta'\pi$ channel it was six partial waves, namely $(L = 1,\ldots,6; M = 1)$. All the waves describing the $\eta^{(\prime)}\pi$ system have positive reflectivity $\epsilon = +$. In the Regge asymptotic limit, reflectivity coincides with naturality of the exchange; at the nucleon vertex, the natural $I\!P$ and f_2 are the dominant exchanges [19]. A single negative reflectivity wave was included in the fit, $(L, M, \epsilon) = (0, 0, -)$, that includes possible reducible backgrounds, was found to contribute at the 0.5% (1.1%) level to the total $\eta\pi$ ($\eta'\pi$) intensity, and will be neglected here.

The partial waves in Eq. (2) are written as

$$f_{LM}(m) = \sqrt{I_{LM}(m)}\, e^{i\delta_{LM}(m)}\,, \qquad (3)$$

where $I_{LM}(m)$ are the partial wave intensities and the phases $\delta_{LM}(m)$ are determined with respect to the phase of the $L = 2, M = 1$ wave, *i.e.* $\delta_{21}(m) \equiv 0$. In our analysis, we use the intensities and phases provided in the corrigendum to Ref. [9]. The simplest way to compare the COMPASS results with a theoretical model would be to compare the partial waves. However, for reasons that will be discussed later in Section IV, we instead fit our amplitude model using an integral form of extended negative log-likelihood (ENLL) method [20–22] to the intensity $I(m,\Omega)$ reconstructed from the partial waves. There are two ways to reconstruct the $I(m,\Omega)$ from the COMPASS partial waves. One approach is to use the mean values of the intensity and phase at a given m, and use Eq. (2) to obtain $I(m,\Omega)$. We call this the mean value reconstruction (MVR). However, this method ignores the experimental uncertainties. The second method, which we refer to as MCR, uses Monte Carlo reconstruction. This is done by associating a probability distribution to the intensity and phase at each m independently. In doing so, instead of a single intensity value for each $(m,\phi,\cos\theta)$ point, we obtain a distribution. We can then compute the expected (mean) value of the intensity and its associated uncertainty at a given confidence level. The statistical errors are thus propagated from the partial waves to the intensity. The details on the MCR can be found in Appendix B. What remains unknown, however, are the uncertainties associated to the systematics of the COMPASS fit and the correlations among partial waves. As a consequence, the intensities reconstructed using MVR and MCR differ.

In Figs. 1 and 2 we show the density plots of $I(m,\Omega)$ at three fixed m as well as the ϕ-integrated distributions

$$I_\theta(m,\cos\theta) = \int_0^{2\pi} \mathrm{d}\phi\, I(m,\Omega)\,. \qquad (4)$$

In Fig. 3 we plot $I_\theta(m,\cos\theta)$ for m above 2.3 GeV, for a total of seventeen mass bins in each channel. This

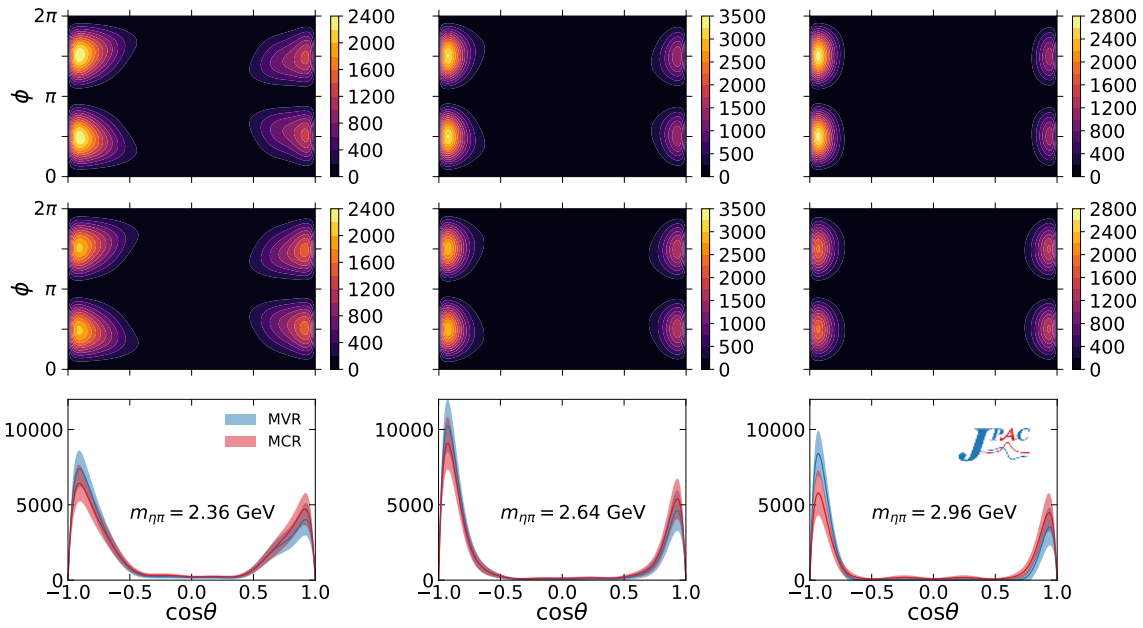

FIG. 1. $\cos\theta$ vs. ϕ expected value intensity $I(m_{\eta\pi}, \Omega)$ density plot for MVR (upper) and MCR (center) of the COMPASS partial waves of the $\eta\pi$ channel for three fixed energies ($m_{\eta\pi} = 2.36$, 2.64, and 2.96 GeV). The lower row provides the ϕ-integrated $I_\theta(m_{\eta\pi}, \cos\theta)$ MVR (blue) and MCR (red) 1σ bands. Since the MVR does not propagate uncertainties, we show as MVR error bands the same computed from the MCR.

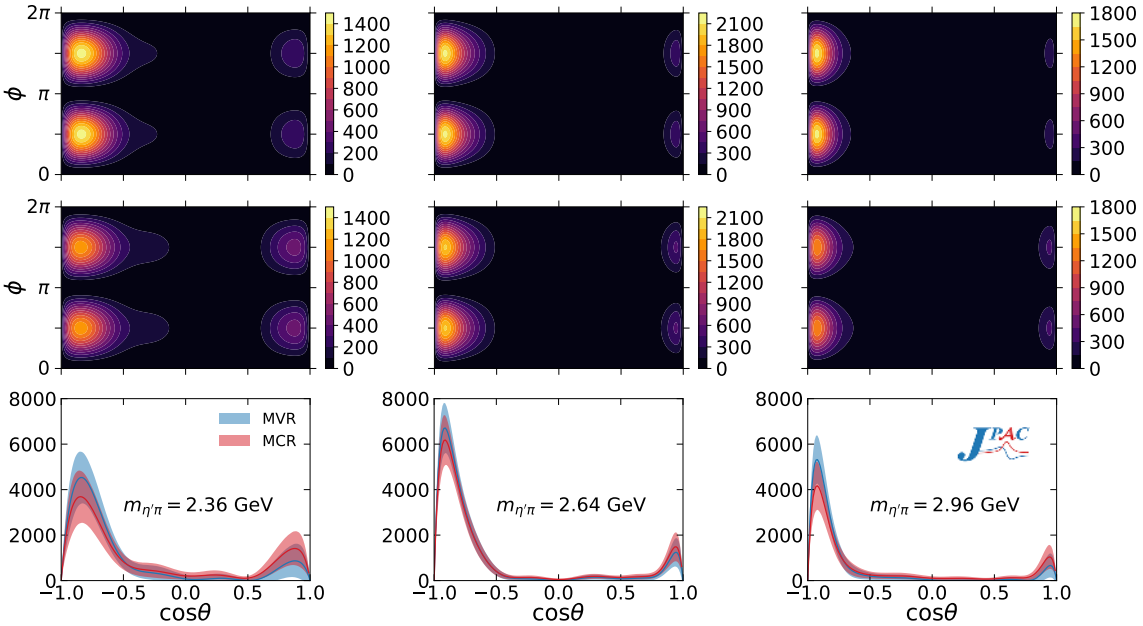

FIG. 2. Same as Fig. 1 for $\eta'\pi$. We note that the $\eta'\pi$ backward peak is broader than the $\eta\pi$ one and that the forward-backward asymmetry is more pronounced.

can be compared to the plot of the experimental data shown in Fig. 2 of Ref. [9], although we note that the data shown in the COMPASS paper are not corrected for detector acceptance. Several features in Figs. 1, 2, and 3 are noteworthy:

1. At fixed m, the intensity $I(m, \Omega)$ is periodic in ϕ with periodicity 2π. Moreover, it presents a reflection symmetry along the azimuthal angle ϕ with symmetry axis at $\phi = \pi$, *i.e.* $I(m, \theta, \phi) = I(m, \theta, 2\pi - \phi)$ with $\phi \in [0, 2\pi]$. Both facts stem from the definition of the intensity, Eq. (2);

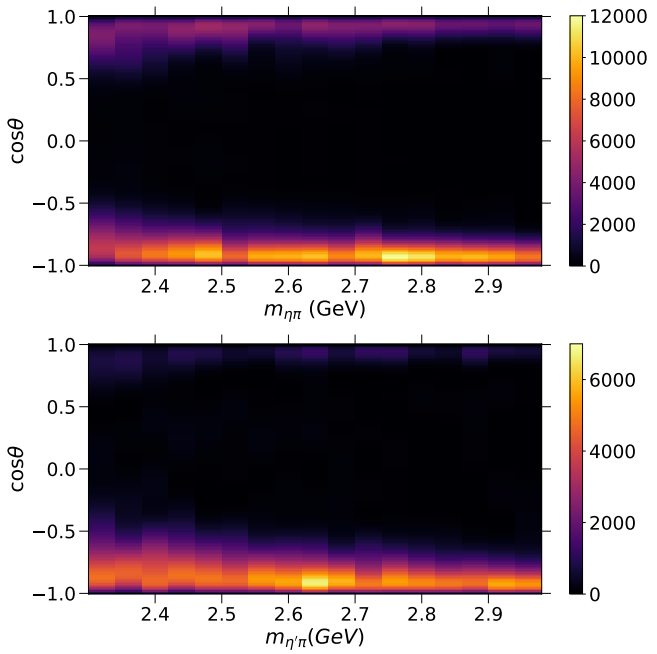

FIG. 3. Intensity $I_\theta(m, \cos\theta)$ density distribution of the MVR from the $\eta\pi$ (upper) and $\eta'\pi$ (lower) COMPASS partial waves.

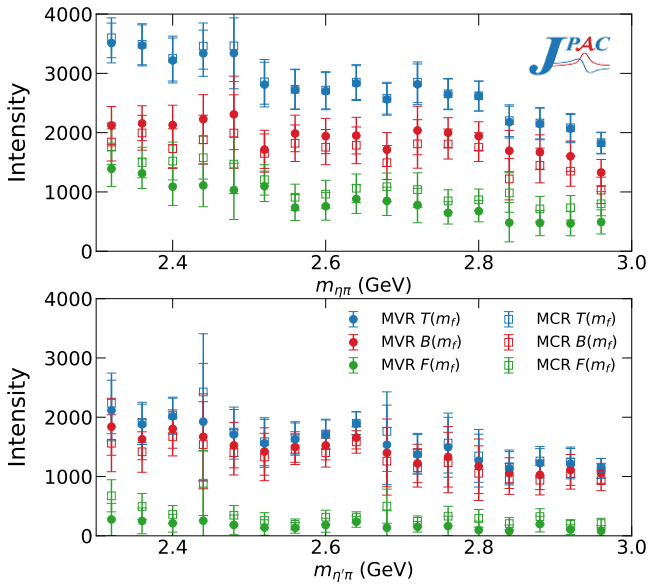

FIG. 4. Integrated forward $F(m)$ (green), backward $B(m)$ (red), and total $T(m) = F(m) + B(m)$ (blue) intensities as defined in Eq. (5) for the MVR (full circles) and MCR (empty squares). Uncertainties in the MVR are taken from the MCR. We note that the slope of $F(m)$ for both $\eta\pi$ and $\eta'\pi$ is steepper than for $B(m)$.

2. the intensity peaks in the forward $\cos\theta \sim 1$ and backward $\cos\theta \sim -1$ regions. In the forward region, most of the beam momentum is carried by the $\eta^{(\prime)}$, and in the backward region by the π. We call these clusters the "fast-η" and the "fast-π" regions, respectively;

3. the backward (fast-π) peak is larger than the forward (fast-η) peak, resulting in a forward-backward asymmetry. This effect is more pronounced in the case of the $\eta'\pi$ channel;

4. the backward peak is broader in $\eta'\pi$ than in the $\eta\pi$;

5. both the forward and backward peaks become narrower as the invariant mass m increases;

6. the MVR intensities at backward peak are larger than those of the MCR, and in the small $|\cos\theta|$ region the intensity profile becomes smeared out in the MCR, so more structures are visible in the MVR in the region where intensities are low. Appendix C provides more insight on the differences between MVR and MCR.

These features are typical of diffractive processes, indicating the dominance of double-Regge exchanges in the energy region $m \gtrsim 2.3\,\text{GeV}$. In the $SU(3)$ flavor symmetric limit the π and the octet η_8 are degenerate, and so are the a_2 and f_2 Regge trajectories. Furthermore, if the $SU(3)$ singlet exchanges (*e.g.* the $I\!P$) are neglected, the forward and backward intensities are identical [23] for the production of the octet, and only even (nonexotic) waves contribute. Since η' is dominated by the $SU(3)$ singlet we expect the asymmetry to be larger for the production of $\eta'\pi$. The broadness of the peaks is related to the relative strength of the different double-Regge contributions to the amplitudes and will be addressed in Sections V and VI.

To quantify the forward-backward asymmetry we define

$$F(m) \equiv \int_0^1 \mathrm{d}\cos\theta\, I_\theta(m, \cos\theta)\,, \tag{5a}$$

$$B(m) \equiv \int_{-1}^0 \mathrm{d}\cos\theta\, I_\theta(m, \cos\theta)\,, \tag{5b}$$

$$A(m) \equiv \frac{F(m) - B(m)}{F(m) + B(m)}\,, \tag{5c}$$

with $F(m)$ and $B(m)$ being the forward and backward intensities, respectively, and $A(m)$ the forward-backward asymmetry. Figure 4 shows $F(m)$, $B(m)$, and their sum $T(m)$ for both MVR and MCR for the two channels. We find that the slope of $F(m)$ is steeper than that of $B(m)$. These intensities show clearly the difference between the MVR and the MCR, even though the total intensity in the MVR and MCR are similar.

III. DOUBLE REGGE MODEL

We present here a double-Regge exchange model for the reactions in Eq. (1). Multi-Regge exchange formalism has been extensively studied theoretically in the

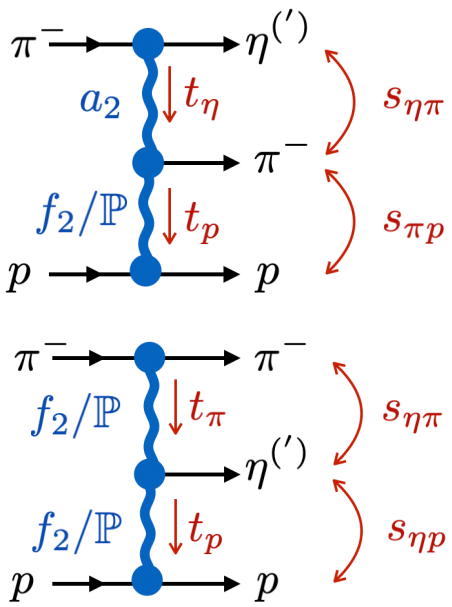

FIG. 5. Fast-η (top) and fast-π (bottom) amplitudes.

past [15, 24–28]. An application of such formalism was presented in [29] for a similar reaction, two-pseudoscalar mesons production in $K^\pm$ and $\pi^\pm$ beam diffraction. More recently the double-Regge exchange was used to describe the central meson production in the high energy proton-proton collisions [30–32]. We will adopt the same model and quote in this section its main features.

The fast-η and fast-π regions correspond to the fast-η and fast-π double-Regge exchange amplitudes depicted in Fig. 5. The model assumes the dominance of leading Regge trajectories. Although it is known that daughter poles and cuts also contribute at finite energies, *i.e.* to polarization observables [33–36], present data are not sensitive to subleading exchanges.

The top exchange is saturated by the a_2 trajectory for the fast-η amplitude, and by the f_2 or $I\!P$ trajectory for the fast-π amplitude. The bottom exchange is either the f_2 or $I\!P$ for both types of amplitude. It is common lore that, at COMPASS energies, the $I\!P$ is the only relevant bottom exchange; however, this hypothesis is incompatible with data, as we will show in Section V.

Consequently, the total amplitude A_{Th} is the sum of six possible double-Regge amplitudes

$$A_{\text{Th}}(m,\Omega) = c_{a_2 I\!P}\, A_{a_2 I\!P} + c_{a_2 f_2}\, A_{a_2 f_2} + c_{f_2 I\!P}\, A_{f_2 I\!P} + c_{f_2 f_2}\, A_{f_2 f_2} + c_{I\!P I\!P}\, A_{I\!P I\!P} + c_{I\!P f_2}\, A_{I\!P f_2}\,, \quad (6)$$

where the $\{c\}$ are unknown and will be fitted to data. The intensity of the model is given by

$$I_{\text{Th}}(m,\Omega) = k(m)\,|A_{\text{Th}}(m,\Omega)|^2, \quad (7)$$

where $k(m) = \lambda^{\frac{1}{2}}(m^2, m^2_{\eta^{(\prime)}}, m^2_\pi)/(2m)$ is the breakup momentum between the π and the $\eta^{(\prime)}$, and $\lambda(x,y,z) = x^2+y^2+z^2-2(xy+xz+yz)$ is the triangle function.

Regge amplitudes are expressed in terms of Lorentz invariants. In addition to s, t_p and m, as depicted in Fig. 5, for the fast-η and π amplitudes, the GJ angles are related to the following Lorentz invariants

$$\text{fast-}\eta: \quad t_\eta = (q-k_\eta)^2, \quad s_{\pi p} = (k_\pi + p_2)^2\,, \quad (8a)$$
$$\text{fast-}\pi: \quad t_\pi = (q-k_\pi)^2, \quad s_{\eta p} = (k_\eta + p_2)^2\,. \quad (8b)$$

There are only five independent variables. The fast-π invariant t_π and $s_{\eta p}$ can be expressed as linear combinations of the five fast-η variables. Appendix A summarizes the relevant kinematical relations.

The analytic structure is the same for all double-Regge amplitudes. The dependence in the momentum transferred (t_η, t_p) for fast-η and (t_π, t_p) for fast-π enters only via the trajectories (α_1, α_2), where α_1 corresponds to the top exchange and α_2 to the bottom one. Hence, for fast-η amplitudes $\alpha_1 \equiv \alpha_{a_2}(t_\eta)$ and for fast-π amplitudes $\alpha_1 \equiv \alpha_{f_2}(t_\pi)$ or $\alpha_1 \equiv \alpha_{I\!P}(t_\pi)$. The bottom trajectory is $\alpha_2 \equiv \alpha_{f_2}(t_p)$ or $\alpha_2 \equiv \alpha_{I\!P}(t_p)$ for both types depending on the bottom exchange.

Regge theory predicts the dependence in the invariant masses squared (s_1, s_2) with $(s_1, s_2) = (s_{\eta\pi}, s_{\pi p})$ for the fast-η amplitudes and $(s_1, s_2) = (s_{\eta\pi}, s_{\eta p})$ for the fast-π amplitudes. Since the nucleons play a spectator role given the large total energy, their spins can be ignored. For five spinless particles with an odd number of pseudoscalars, the generic amplitude for a double-Regge exchange is [15, 29]

$$T(\alpha_1,\alpha_2;s_1,s_2) = K\,\Gamma(1-\alpha_1)\,\Gamma(1-\alpha_2)\,\frac{(\alpha' s_1)^{\alpha_1}(\alpha' s_2)^{\alpha_2}}{\alpha' s}\left[\frac{\xi_1\,\xi_{21}}{\kappa^{\alpha_1}}\,V(\alpha_1,\alpha_2,\kappa) + \frac{\xi_2\,\xi_{12}}{\kappa^{\alpha_2}}\,V(\alpha_2,\alpha_1,\kappa)\right]. \quad (9)$$

The double-Regge limit corresponds to $s, s_1, s_2 \to \infty$ with $\kappa^{-1} \equiv s/(\alpha' s_1 s_2)$ fixed, which is related to the cosine of the Toller angle [15]. We set the scale parameter $\alpha' = 0.8\,\text{GeV}^{-2}$. Changing this value induces a smooth exponential dependence on the momentum transfer variables. We have found that fitting simultaneously $\{c\}$ and α' does not lead to stable solutions, as the coefficients and the scale parameter are strongly correlated. Moreover, α'

should be of the order of the hadronic scale, $\mathcal{O}(\text{GeV}^{-2})$. We let α' vary in exploratory fits and found the above choice to be optimal. The kinematical factor K is detailed in Appendix A.

The presence of two symmetric terms in the bracket of Eq. (9) is imposed from general considerations of the analytic structure of double-Regge amplitudes. The interested readers will find the technical details in Section 3.3 of Ref. [15].

The double-Regge amplitude of Eq. (9) has poles for positive integer values of the trajectories α_1 and α_2, which are related to the spins of the physical particles in the t channel. Since only poles with even signature $(-1)^J = +1$ can couple to $\eta\pi$ and $\pi\pi$, odd signature poles are removed by the signature factors

$$\xi_n = \frac{1 + e^{-i\pi\alpha_n}}{2}\,, \tag{10a}$$

$$\xi_{nm} = \frac{1 + e^{-i\pi(\alpha_n - \alpha_m)}}{2}\,. \tag{10b}$$

The vertex function $V(\alpha_1, \alpha_2, \kappa)$ is an analytic function of its arguments. Its most general form involves an infinite number of Reggeon-Reggeon-particle couplings and reduces to a polynomial in κ^{-1} for integer α_1 and α_2 [24]. In a dual model, all Reggeon-Reggeon-particle couplings are equal and the vertex simplifies to [15, 37]

$$V(\alpha_1, \alpha_2, \kappa) = \frac{\Gamma(\alpha_1 - \alpha_2)}{\Gamma(1 - \alpha_2)}\, {}_1F_1\left(1 - \alpha_1, 1 - \alpha_1 + \alpha_2, -\kappa\right)\,, \tag{11}$$

where ${}_1F_1$ is the confluent hypergeometric function of the first kind.

As explained in Ref. [29], the $V(\alpha_1, \alpha_2, \kappa)$ functions used in Eq. (9) and defined in Eq. (11) have poles at $\alpha_1 - \alpha_2$ (and $\alpha_2 - \alpha_1$ for $V(\alpha_2, \alpha_1, \kappa)$) equal to non-positive integers. However, these poles cancel between the two terms in Eq. (9). For example, when $\alpha_2 > \alpha_1$ the pole in the gamma function in Eq. (11) cancels out with the pole in the hypergeometric function from the second term Eq. (9).

The six contributions in Eq. (6) are obtained from the generic double-Regge amplitude (9) with the following substitutions:

$$A_{a_2\mathbb{P}} = T(\alpha_{a_2}(t_\eta), \alpha_{\mathbb{P}}(t_p); s_{\eta\pi}, s_{\pi p})\,, \tag{12a}$$

$$A_{a_2 f_2} = T(\alpha_{a_2}(t_\eta), \alpha_{f_2}(t_p); s_{\eta\pi}, s_{\pi p})\,, \tag{12b}$$

$$A_{f_2\mathbb{P}} = T(\alpha_{f_2}(t_\pi), \alpha_{\mathbb{P}}(t_p); s_{\eta\pi}, s_{\eta p})\,, \tag{12c}$$

$$A_{f_2 f_2} = T(\alpha_{f_2}(t_\pi), \alpha_{f_2}(t_p); s_{\eta\pi}, s_{\eta p})\,, \tag{12d}$$

$$A_{\mathbb{P}\mathbb{P}} = T(\alpha_{\mathbb{P}}(t_\pi), \alpha_{\mathbb{P}}(t_p); s_{\eta\pi}, s_{\eta p})\,, \tag{12e}$$

$$A_{\mathbb{P} f_2} = T(\alpha_{\mathbb{P}}(t_\pi), \alpha_{f_2}(t_p); s_{\eta\pi}, s_{\eta p})\,. \tag{12f}$$

Since the momentum transferred between the initial and final nucleon has been integrated over in the COMPASS analysis, we do not have access to the t_p distribution. This distribution would allow us to discriminate between the bottom exchanges. Since the amplitude decreases exponentially with t_p, we fix t_p close to the COMPASS lowest limit, $t_p = -0.2\,\text{GeV}^2$. Results are stable against small variation of this value.

Finally, we need to specify the Regge trajectories

$$\alpha_{a_2}(t) = 0.53 + 0.90\,t, \tag{13a}$$

$$\alpha_{f_2}(t) = 0.47 + 0.89\,t, \tag{13b}$$

$$\alpha_{\mathbb{P}}(t) = 1.08 + 0.25\,t, \tag{13c}$$

where we adopted the standard parametrization for the $\mathbb{P}$ [38] and the f_2 [39] trajectories. Phenomenologically, the a_2 trajectory is very similar to that of ρ, which is referred as exchange degeneracy (EXD) [28, 40]. Our model is thus entirely specified by the six real parameters $\{c\}$. Each $\{c\}$ in Eq. (6) is a product of two particle-Reggeon-particle couplings (top and bottom vertices) and one Reggeon-particle-Reggeon coupling (middle vertex). The particle-Reggeon-particle couplings could be extracted from quasi-two-body reactions [41, 42], but the Reggeon-particle-Reggeon couplings are largely unknown. In principle, all couplings have residual dependence on t's that cannot be disentangled. This prevents us from imposing further relations among the η and η' amplitude parameters.

IV. PARTIAL WAVE TRUNCATION BEYOND THE RESONANCE REGION

COMPASS extracted partial waves under the assumption that only a limited number of them contribute. This is justifiable in the resonance region, but as the invariant mass of the $\eta^{(\prime)}\pi$ system increases so does the number of relevant waves. Since the overall intensity decreases in the high energy region, the significance of higher waves ($L > 6$) could not be established and, hence, they were neglected.

The Regge model developed in the previous Section is not based on a partial wave expansion and therefore implicitly includes all partial waves. One can thus study whether the approximation to truncate to $L \leqslant 6$ waves is appropriate for our model. In Fig. 6 we show how the truncation affects the total intensity in the $\eta\pi$ channel. We expand each amplitude into partial waves and then sum back only the ones considered in the COMPASS analysis. For example, at $m_{\eta\pi} = 2.64\,\text{GeV}$, the seven partial waves considered by COMPASS account for $\sim 80\%$ of the intensity at the peak for the f_2/f_2 exchange. At this $m_{\eta\pi}$, only for the $\mathbb{P}/\mathbb{P}$ and $\mathbb{P}/f_2$ amplitudes this truncation adequately reproduces the intensity ($> 99\%$ and $> 97\%$, respectively). If we include the partial waves up to $L = 10$ with $M = 1$ and $M = 2$, the intensity of the amplitudes is almost completely recovered ($> 99\%$ for all amplitudes except for a_2/f_2, which is $> 93\%$). In Fig. 7 we show the same plots for the $\eta'\pi$ channel. In this case, the main disagreement happens in the forward peak ($a_2/\mathbb{P}$ and a_2/f_2 amplitudes), where only between

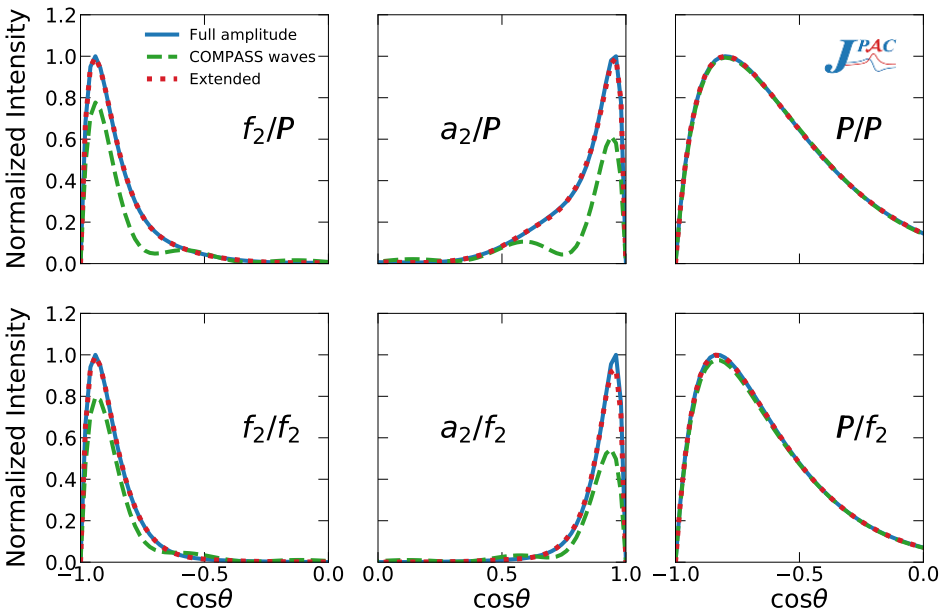

FIG. 6. $I_\theta(m_{\eta\pi}, \cos\theta)$ for individual amplitudes at $m_{\eta\pi} = 2.64\,\text{GeV}$ for the $\eta\pi$ channel. We compute the intensity of each individual amplitude (solid blue) normalized to its peak value. We compare it to two different partial wave truncations. The dashed green curve adds up the partial waves included in the COMPASS analysis, *i.e.* $(L; M) = (1, \ldots, 6; 1)$ and $(2; 2)$. The dotted red curve is obtained by extending the sum to $(L; M) = (1, \ldots, 10; 1, 2)$. One can appreciate that, while the COMPASS partial waves saturate the $I\!P/I\!P$ and $I\!P/f_2$, they only account for $\sim 80\%$ of the $a_2/I\!P$ peak intensity.

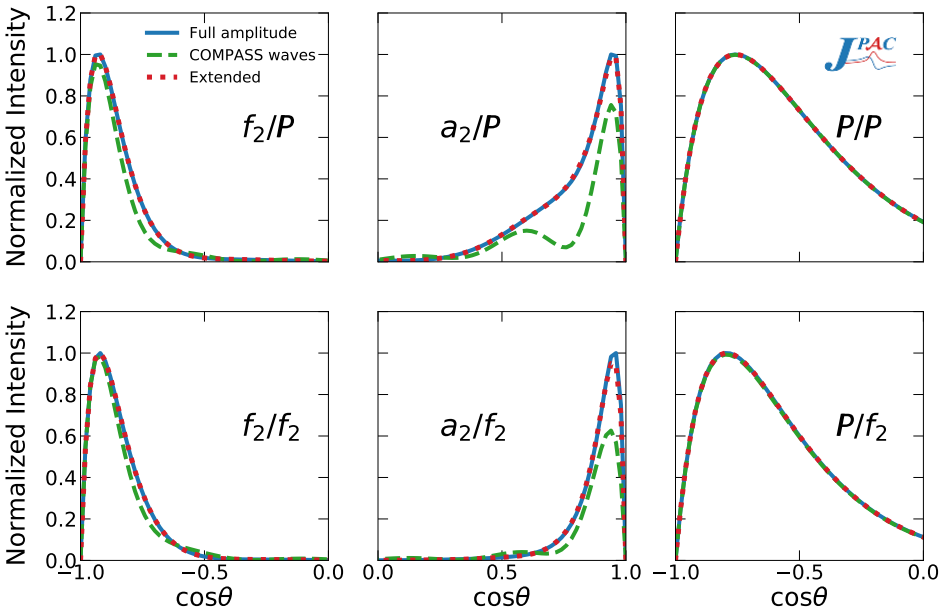

FIG. 7. $I_\theta(m_{\eta'\pi}, \cos\theta)$ for individual amplitudes at $m_{\eta'\pi} = 2.64\,\text{GeV}$ for the $\eta'\pi$ channel. Conventions are the same as in Fig. 6, except that here $(L; M) = (2; 2)$ is not included in the COMPASS waves. Again, the COMPASS partial waves saturate the $I\!P/I\!P$ and $I\!P/f_2$, but only account for $\sim 60\%$ of the a_2/f_2 peak intensity.

60% and 80% of the peak strength is accounted for by the COMPASS partial waves.

Thus, as mentioned earlier, in this energy region COMPASS waves should be considered as an effective parametrization of the data, rather than being directly compared with genuine partial waves from a model that contains an infinite number of waves. However, given that they have been extracted under the constraint of summing up to the total intensity, we can reconstruct $I(m, \Omega)$ from the partial waves using Eq. (2) with the

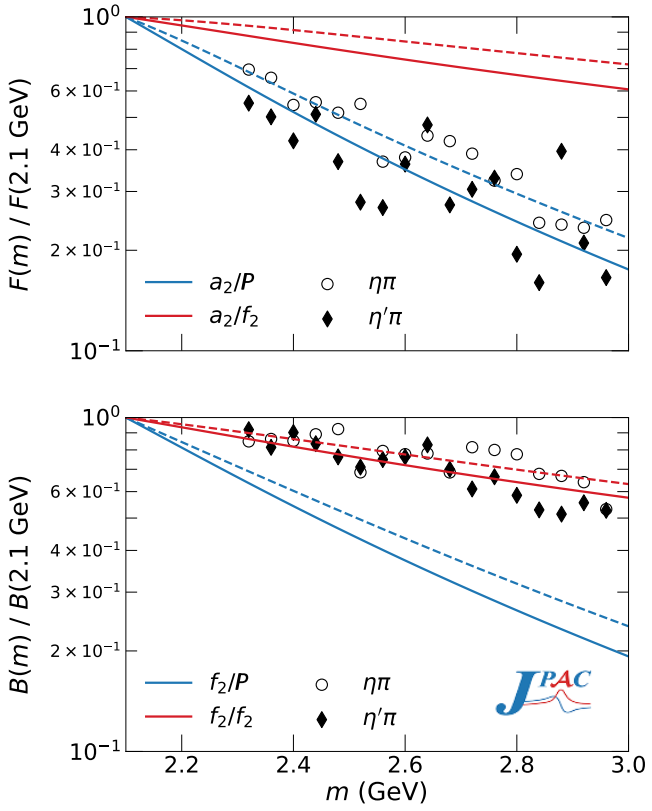

FIG. 8. Forward (upper) and backward (lower) intensities as defined in Eq. (5) for the top-a_2 and top-f_2 amplitudes, respectively. Solid lines correspond to $\eta\pi$ and dashed to $\eta'\pi$. Each theoretical intensity is normalized to its value at $m = 2.1\,\text{GeV}$. In circles and diamonds we show the experimental data arbitrarily rescaled, as obtained by MVR.

two methods (MVR and MCR) explained in Section II and fit them with our model. In Section VII we will discuss how the model partial waves compare to the f's extracted from the data by COMPASS.

V. THE MINIMAL SET OF AMPLITUDES

Our model described in Section III is completely determined by the six coefficients of the double-Regge exchange amplitudes. As a first approach, we fitted the intensity with all the six parameters unconstrained. However, those fits did not lead to a unique solution, sometimes having coefficients compatible with zero. The error estimation was unreliable. In order to make the fits to reach stable solutions, we have to restrict the parameters to at most four. Consequently, to establish which amplitudes must be neglected or included in the fits, in this Section we compare the angular and mass dependencies of the individual exchanges to the experimental ones from MVR shown in Figs. 1–4. Conclusions are identical for MCR.

In the $SU(3)$ limit, the event distribution of $\eta\pi$ becomes symmetric in $\cos\theta$. At the amplitude level, this is manifested via EXD, meaning that the parameters of the a_2 and f_2 Regge poles are equal, including the couplings, $c_{a_2\mathbb{P}} \simeq -c_{f_2\mathbb{P}}$ and $c_{a_2 f_2} \simeq -c_{f_2 f_2}$.[1] Deviations from the EXD relation are manifested in the nonvanishing forward-backward asymmetry. The $\cos\theta$ dependence is correlated to the t_π or t_η dependence arising from the top exchange trajectory. We thus expect the amplitudes with the same top exchange to have similar $\cos\theta$ behavior. Both a_2/f_2 and $a_2/\mathbb{P}$ amplitudes will be collectively denoted as top-a_2 amplitudes, and similarly for the top-f_2 and top-$\mathbb{P}$ amplitudes. By EXD, we expect that both top-a_2 and -f_2 matter.

As shown in Figs. 6 and 7, the top-a_2 and top-f_2 amplitudes produce a narrow forward and a narrow backward peak, respectively. The top-$\mathbb{P}$ amplitudes produce a wider backward peak, which is due to the smaller slope of the $\mathbb{P}$ trajectory. Given that the widths of the experimental backward peaks in $\eta\pi$ and $\eta'\pi$ are similar to what is expected from the top-f_2 exchange, we conclude that the f_2/f_2 and/or $f_2/\mathbb{P}$ amplitudes should account for most of the backward intensity. The residual contribution from the $\mathbb{P}/\mathbb{P}$ and $\mathbb{P}/f_2$ amplitudes may be needed to further widen the peak. In particular, the top-$\mathbb{P}$ contributions might be necessary for the $\eta'\pi$ channel.

We next investigate the mass dependence of the top-a_2 and top-f_2 amplitudes. In Fig. 4 we find that $F(m)$ is steeper than $B(m)$. The slope of the distribution is determined by the slopes of the trajectories in Eq. (13) of both top and bottom exchanges, once the angular variables have been integrated over. The m dependence for individual amplitudes in Fig. 8 shows this effect. A steeper slope of the intensity is observed when the bottom exchange is $\mathbb{P}$. Hence, the steeper $F(m)$ favors a bottom-$\mathbb{P}$, while the flatter $B(m)$ a bottom-f_2. Consequently, both the $a_2/\mathbb{P}$ and f_2/f_2 amplitudes should be included.

Another important feature is the ϕ dependence. In Fig. 9 we compare the ϕ dependence in the forward region of $I(m,\Omega)$ and the top-a_2 amplitudes. We see that a single amplitude cannot reproduce the experimental distributions at all m. Therefore, we will include both a_2/f_2 and $a_2/\mathbb{P}$ amplitudes in our fits.

In Fig. 10 we make the same comparison for the backward region. The $f_2/\mathbb{P}$ and $\mathbb{P}/f_2$ amplitudes do not peak at the correct position at any m. On the other hand, the f_2/f_2 and the $\mathbb{P}/\mathbb{P}$ match better the data. As explained above, the f_2/f_2 amplitude is already favored by the observed $B(m)$ slope.

In conclusion, the minimal set of amplitudes (MIN) common to both channels, consists of $a_2/\mathbb{P}$, a_2/f_2, and f_2/f_2.

Additionally, as discussed earlier, we may extend this set in order to take into account the width of the backward peak. In particular, the $\eta'\pi$ peak is broader than

[1] The minus sign is due to the kinematic factor K being odd under permutation of the π and η momenta.

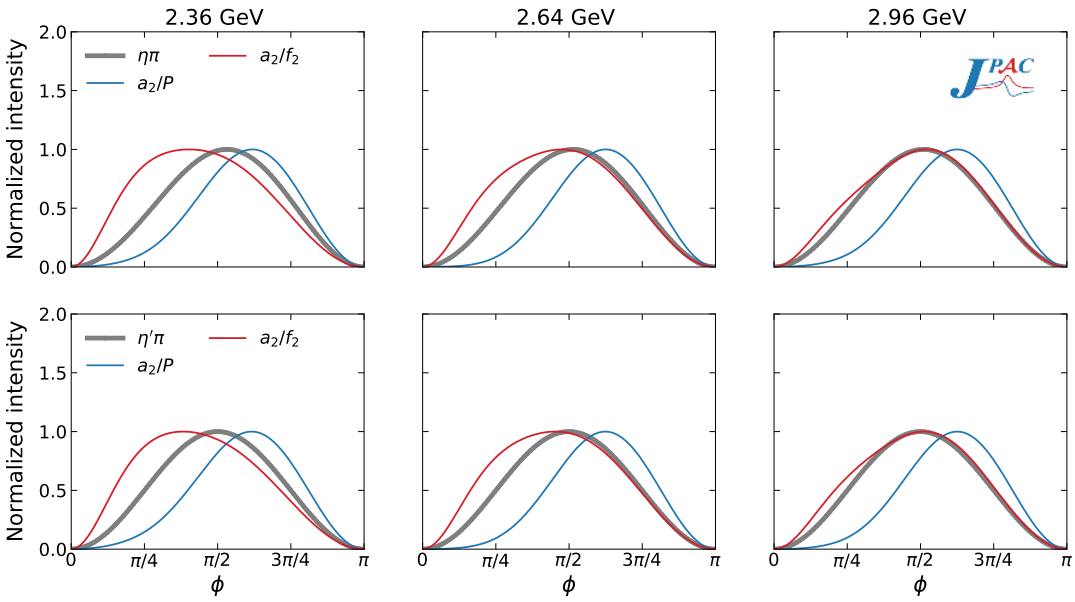

FIG. 9. Intensity distribution of ϕ from MVR (grey), for three fixed energies and $\cos\theta = 0.866$ (close to the forward peak) for $\eta\pi$ (upper row) and $\eta'\pi$ (lower row) compared to the same distributions for the $a_2/I\!P$ (blue) and a_2/f_2 (red) amplitudes. Each distribution is normalized to its peak value. Due to the reflection symmetry shared by the model and the intensity, we only show $\phi \in [0, \pi]$.

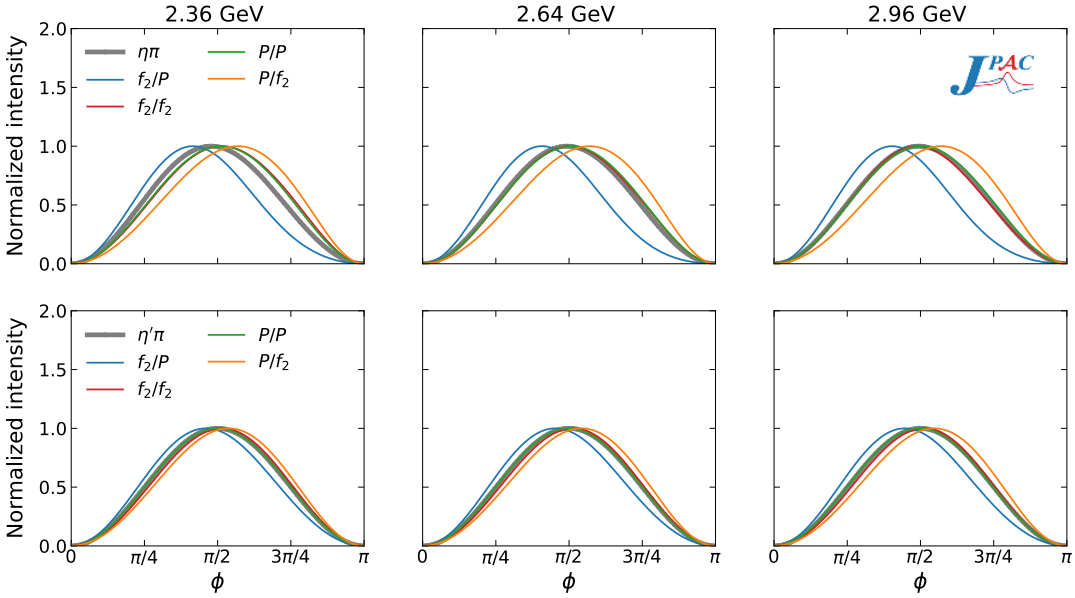

FIG. 10. Intensity distribution of ϕ from MVR (grey), for three fixed energies and $\cos\theta = -0.866$ (close to the backward peak) for $\eta\pi$ (upper row) and $\eta'\pi$ (lower row) compared to the same distributions for the $f_2/I\!P$ (blue), f_2/f_2 (red), $I\!P/I\!P$ (green), and $I\!P/f_2$ (orange) amplitudes. Each distribution is normalized to its peak value.

predicted by the f_2/f_2 amplitude. Including the $I\!P/f_2$ would help. However, it may disrupt the ϕ distribution as shown in Fig. 10. An option would be to include both $I\!P/f_2$ and $f_2/I\!P$. However, as stated earlier in this Section, including more than four amplitudes makes the fits unstable. For this reason we do not include the $I\!P/f_2$ amplitude in any fits.

Therefore, we are left with two options to broaden the backward peak: either $I\!P/I\!P$ or $f_2/I\!P$. The $I\!P/I\!P$ amplitude allows to broaden the backward peak without affecting much the ϕ dependence. It also would make the backward peak broader than the $f_2/I\!P$ exchange. The $f_2/I\!P$ exchange shifts the ϕ distribution to peak below $\pi/2$, but by interfering with f_2/f_2 this shift may be re-

duced. Hence, we explore adding either the $f_2/I\!P$ or $I\!P/I\!P$ amplitudes to the MIN set for fitting the intensities.

To summarize, the sets of amplitudes we explore are:

(i) MIN, that includes the $a_2/I\!P$, a_2/f_2 and f_2/f_2 amplitudes, *i.e.* parameter set $\{c_{a_2 I\!P}, c_{a_2 f_2}, c_{f_2 f_2}\}$;

(ii) MIN+$f/I\!P$, with parameter set $\{c_{a_2 I\!P}, c_{a_2 f_2}, c_{f_2 I\!P}, c_{f_2 f_2}\}$;

(iii) MIN+$I\!P/I\!P$, with parameter set $\{c_{a_2 I\!P}, c_{a_2 f_2}, c_{f_2 f_2}, c_{I\!P I\!P}\}$.

VI. RESULTS

A. Extended negative log-likelihood fit

The contribution of each amplitude in a given set (MIN, MIN+$f/I\!P$, and MIN+$I\!P/I\!P$) is determined by fitting the MVR and the MCR distributions for each $\eta^{(\prime)}\pi$ channel independently.

We first discuss how to fit the MVR. In each mass bin, the intensity $I(m,\Omega)$ depends on two angles $\Omega = (\phi, \cos\theta)$. The continuous variables prevent us from using a standard χ^2 fit. Besides, we need to take into account the fact that the total intensity is a fixed quantity. Hence, we use an integral form of the extended negative log-likelihood function (ENLL) [20, 21]:

$$\mathcal{L}(\{c\}) = \sum_i \int \mathrm{d}\Omega \, [I_{\mathrm{Th}}(m_i,\Omega|\{c\}) - I_{\mathrm{Exp}}(m_i,\Omega) \log I_{\mathrm{Th}}(m_i,\Omega|\{c\})] \,, \qquad (14)$$

where the experimental intensity $I_{\mathrm{Exp}}(m,\Omega)$ is the fitting objective function computed using Eq. (2) with MVR, and the theoretical intensity $I_{\mathrm{Th}}(m,\Omega|\{c\})$ is computed from Eq. (7). The experimental distributions are fitted simultaneously in 15 bins of $\{m\}$, in the range $2.38 < m < 2.98\,\mathrm{GeV}$. Varying slightly this interval leaves the results unchanged. We minimize $\mathcal{L}$ using MINUIT [43] to obtain the $\{c\}$ parameters weighting each theoretical amplitude.

We note that the ENLL makes the total intensity of the model as close as possible to the total intensity of data. We remind the normalization of data is unknown, thus the $\{c\}$ cannot be directly compared to normalized couplings. The overall sign of the amplitude is also undetermined, so we fix $c_{a_2 I\!P}$ to be positive. As said above, we expect $c_{f_2 I\!P}$ to be negative. The best fits found are reported in Table I. Local minima that do not follow the sign expectations were found, although with worse $\mathcal{L}$ than the reported best fit values.

We note that the absolute value of the parameters is not a measure of the importance of any given amplitude contribution, because the A's in Eq. (12) have largely different magnitudes. In particular, bottom-$I\!P$ are much larger than bottom-f_2.

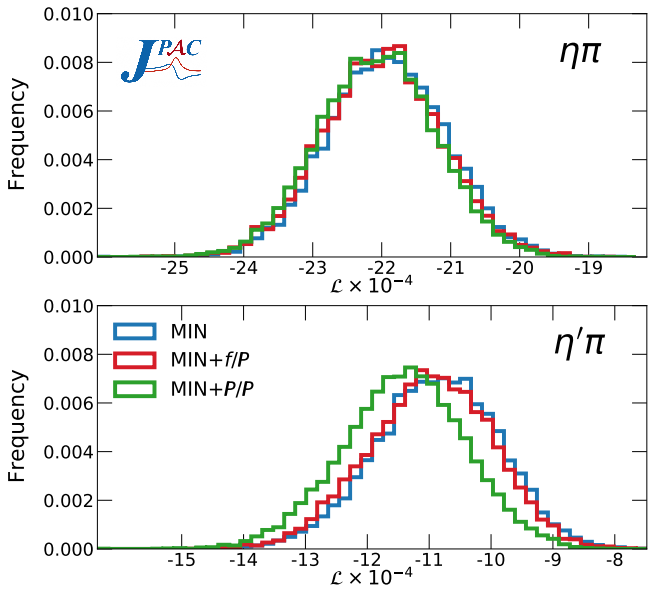

FIG. 11. ENLL $\mathcal{L}_{\mathrm{MCR}}$ distributions for the 10^4 bootstrap fits with the three models to the MCR distributions for $\eta\pi$ (upper) and $\eta'\pi$ (lower) channels.

Fitting the MCR is more challenging. Each pseudodataset j is fitted using Eq. (14), obtaining an independent set of parameters $\{c\}^j$. We estimate the expectation value of the parameters by averaging over $N = 10^4$ fits and the uncertainties from the appropriate quantiles. This number of pseudodatasets allows us to obtain the probability distribution of each parameter and the correlations with a 2% statistical uncertainty (more details Appendix B).

B. Fit results

Table I gives the value of the ENLL for the three models fitted to the MVR and MCR for both channels, as well as the resulting fit parameters. The distribution of the ENLL for the MCR fits is shown in Fig. 11. We see that the all models have similar ENLL, with a nonsignificant preference for MIN+$I\!P/I\!P$ fit, in particular for the $\eta'\pi$ channel. In Appendix D we analyze this difference more systematically and conclude that, statistically, there is indeed a preference for the MIN+$I\!P/I\!P$ model for the $\eta'\pi$ channel.

In Appendices C and E we compare MVR and MCR observables and fits, respectively, finding that MCR fits are more reliable. Here we summarize the results of the MCR fits and leave the MVR fit results for Appendix E.

1. $\eta\pi$ MCR fits

The three models give consistent values for $c_{a_2 I\!P}$ and $c_{a_2 f_2}$, providing almost identical descriptions of the for-

TABLE I. ENLL and fit parameters $\{c\}$ (in appropriate GeV units) for both MVR and MCR. For MVR, $\mathcal{L}$ corresponds to the best fit found, while for MCR the value and error of $\mathcal{L}$ correspond to the mean value and dispersion of the best ENLL for each pseudodataset. The $\mathcal{L}$ distributions are depicted in Fig. 11, while the parameter distributions are discussed in Appendix F.

Channel		MIN		MIN+$f/I\!P$		MIN+$I\!P/I\!P$	
		MVR	MCR	MVR	MCR	MVR	MCR
$\eta\pi$	$\mathcal{L}\times 10^{-4}$	-22.8	-21.9 ± 0.9	-22.7	-22.0 ± 0.9	-22.8	-22.1 ± 0.8
	$c_{a_2 I\!P}$	0.29	0.42 ± 0.03	0.28	0.40 ± 0.04	0.29	0.36 ± 0.04
	$c_{a_2 f_2}$	3.67	3.3 ± 0.4	3.70	3.4 ± 0.4	3.59	3.8 ± 0.4
	$c_{f_2 I\!P}$	—	—	-0.20	-0.30 ± 0.05	—	—
	$c_{f_2 f_2}$	-11.82	-11.0 ± 0.3	-8.99	-6.6 ± 0.7	-10.86	-8.9 ± 0.4
	$c_{I\!P I\!P}$	—	—	—	—	0.0073	0.0135 ± 0.002
$\eta'\pi$	$\mathcal{L}\times 10^{-4}$	-11.7	-10.9 ± 1.0	-11.7	-11.0 ± 1.0	-11.8	-11.4 ± 1.0
	$c_{a_2 I\!P}$	0.16	0.37 ± 0.07	0.16	0.34 ± 0.05	0.19	0.35 ± 0.05
	$c_{a_2 f_2}$	1.50	0.4 ± 0.6	1.51	0.7 ± 0.5	1.22	0.6 ± 0.5
	$c_{f_2 I\!P}$	—	—	-0.21	-0.29 ± 0.03	—	—
	$c_{f_2 f_2}$	-11.42	-11.0 ± 0.5	-7.73	-5.5 ± 0.7	-9.01	-7.1 ± 0.6
	$c_{I\!P I\!P}$	—	—	—	—	0.012	0.018 ± 0.002

ward peak. This can be appreciated in Fig. 12, where the experimental $I_\theta(m_{\eta\pi},\cos\theta)$ MCR for the fast-η region is compared to the three models for all the fitted $m_{\eta\pi}$ bins. The three models agree very well. Figure 13 shows the same results for the fast-π region. Here the differences among models can be appreciated. As expected from Fig. 6, the MIN+$I\!P/I\!P$ provides a wider peak, and, since the normalization is fixed in a ENLL fit, the maximum intensity at the peak is smaller than the MIN and MIN+$f/I\!P$ results. The latter two fits are similar, with their uncertainty bands overlapping, except in the highest $m_{\eta\pi}$ bin. We note that for some energies the MIN+$I\!P/I\!P$ provides a better description of the experimental distribution, while for others the MIN and MIN+$f/I\!P$ fits look better.

Further insight can be obtained by examining the three-dimensional $I(m_{\eta\pi},\Omega)$ distributions. We define

$$D(m_{\eta\pi},\Omega)=\frac{\bar{I}_{\rm Exp}(m_{\eta\pi},\Omega)-\bar{I}_{\rm Th}(m_{\eta\pi},\Omega)}{\sqrt{\left[\Delta I_{\rm Exp}(m_{\eta\pi},\Omega)\right]^2+\left[\Delta I_{\rm Th}(m_{\eta\pi},\Omega)\right]^2}}\,, \tag{15}$$

where $\bar{I}$ and ΔI are the mean and dispersion of the experimental and theoretical distributions as obtained from MCR.[2] This quantifies point-by-point how similar the MCR and the theoretical distributions are. Figure 14 shows these distributions for the $\eta\pi$ channel in two mass bins. Comparing the model and data distributions, one concludes that the former has more structure in the forward region. The experimental peak has two symmetric blobs in ϕ while the theory is rather asymmetric. As shown in Fig. 9, this is due to the asymmetry in ϕ of the top-a_2 amplitudes. We remind that the symmetry of the experimental ϕ distribution is exact and stems from Eq. (2). This symmetry is not imposed in the model, and is approximately reached by having both top-a_2 amplitudes interfering. All the three models peak at roughly the correct $\phi=\pi/2$ and $3\pi/2$. The situation is different for the backward peak. The MIN fit peaks slightly below (above) the experimental value of $\phi=3\pi/2$ ($\phi=\pi/2$). Hence, we do not favor the MIN model, *i.e.* the f_2/f_2 amplitude is not enough to reproduce the ϕ dependence of the fast-π region.

From the bootstrap fits, we can study the parameter distributions and their correlations, summarized in Appendix F. The correlations confirm that the fast-π and fast-η amplitudes are essentially independent. The parameters are generally well determined and exhibit Gaussian behavior, except the $I\!P/I\!P$ coefficient $c_{I\!P I\!P}$ that has a bimodal distribution.

Finally, although including a bottom-$I\!P$ amplitude is necessary to describe the backward region, data do not show a clear preference for either MIN+$f/I\!P$ or MIN+$I\!P/I\!P$. Since the two models point to different values for the f_2/f_2 coupling, the latter cannot be determined unambiguously either. Currently, we do not have enough precision in the data to determine the con-

[2] We do not take into account the fact that both the theoretical and experimental distributions are evaluated out of the same pseudodatasets, and therefore correlated. However, this still gives a qualitative description of the discrepancy between theory and experiment.

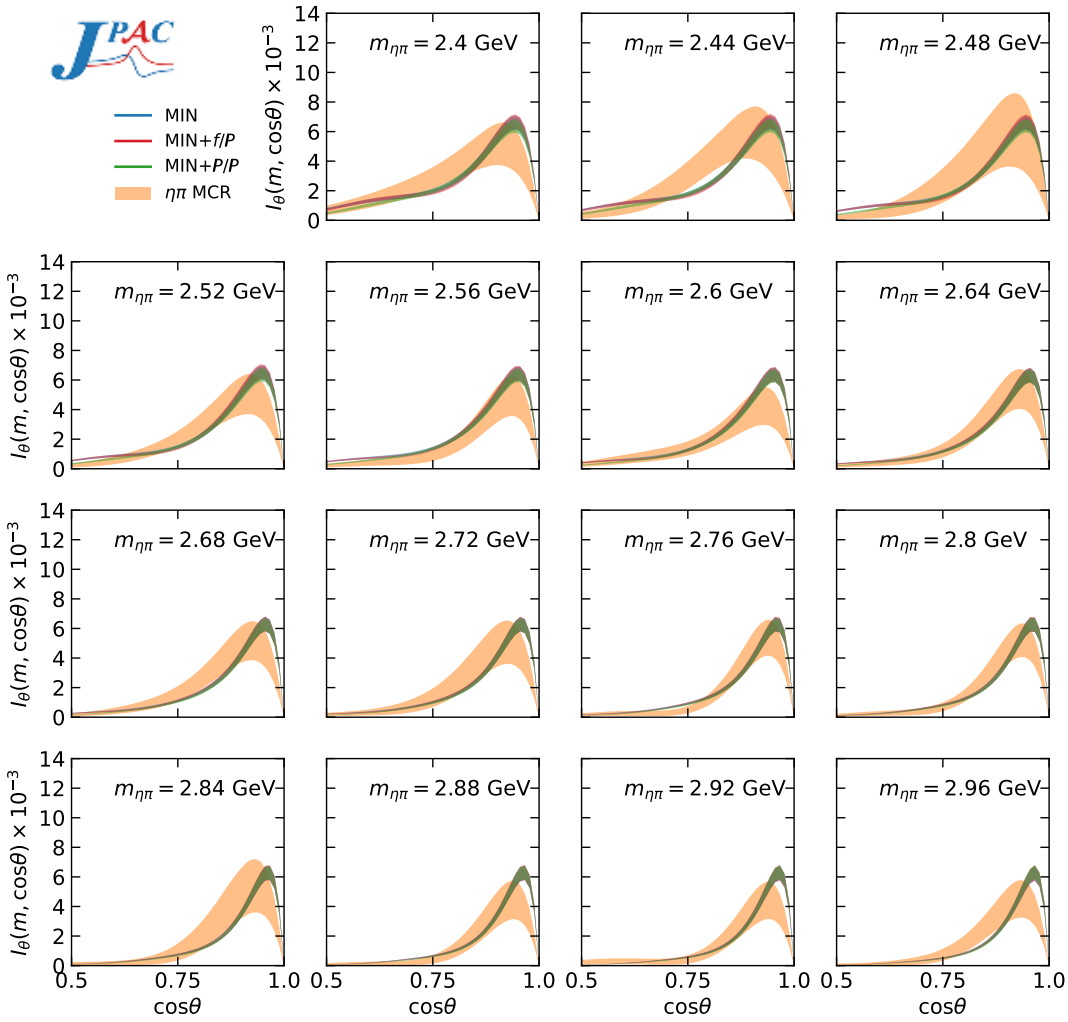

FIG. 12. Experimental $I_\theta(m_{\eta\pi}, \cos\theta)$ from MCR (orange) for the forward region compared to the MIN (blue), MIN+$f/I\!P$ (red) and MIN+$I\!P/I\!P$ (green) fits. Bands correspond to the 68% confidence level. The three model curves mostly overlap.

tributions from the individual exchanges in the backward region.

2. $\eta'\pi$ MCR fits

The fit parameters for the three models are presented in the MCR columns of Table I. As for $\eta\pi$, the three models give consistent values for $c_{a_2 I\!P}$ and $c_{a_2 f_2}$, providing almost identical descriptions of the forward peak. However, $c_{a_2 f_2}$ is compatible with zero at a 2σ level. This suggests larger level of EXD breaking in the $\eta'\pi$ channel. Figures 15 and 16, compare the experimental $I_\theta(m_{\eta'\pi}, \cos\theta)$ with the three models in the forward and backward regions, respectively. The models completely agree in the forward region, while the MIN+$I\!P/I\!P$ provides a wider backward peak, in better agreement with the data.

The three-dimensional distributions for $\eta'\pi$ are shown in Figure 17 for the three models and MCR at $m_{\eta'\pi} =$ 2.60 and 2.80 GeV. As for $\eta\pi$, the MIN does not peak at the correct value of ϕ in the backward region. Results and conclusions are qualitatively similar to the $\eta\pi$ channel. In particular, the preference for a MIN+$I\!P/I\!P$ is clear. This points to a large affinity of η' to gluons as discussed in the literature [44].

3. Forward and backward intensities and asymmetry

Figures 18 and 19 show the forward, backward, and total intensities. We show that MIN+$f/I\!P$ for $\eta\pi$ and MIN+$I\!P/I\!P$ for $\eta'\pi$ reproduce all the intensities rather well.

We also note that the integrated forward intensity is systematically larger for the MCR. The opposite is true for the the backward one, which is systematically larger for the MVR. Consequently, the forward-backward asymmetry $A(m)$, defined in Eq. (5c), is, in absolute value,

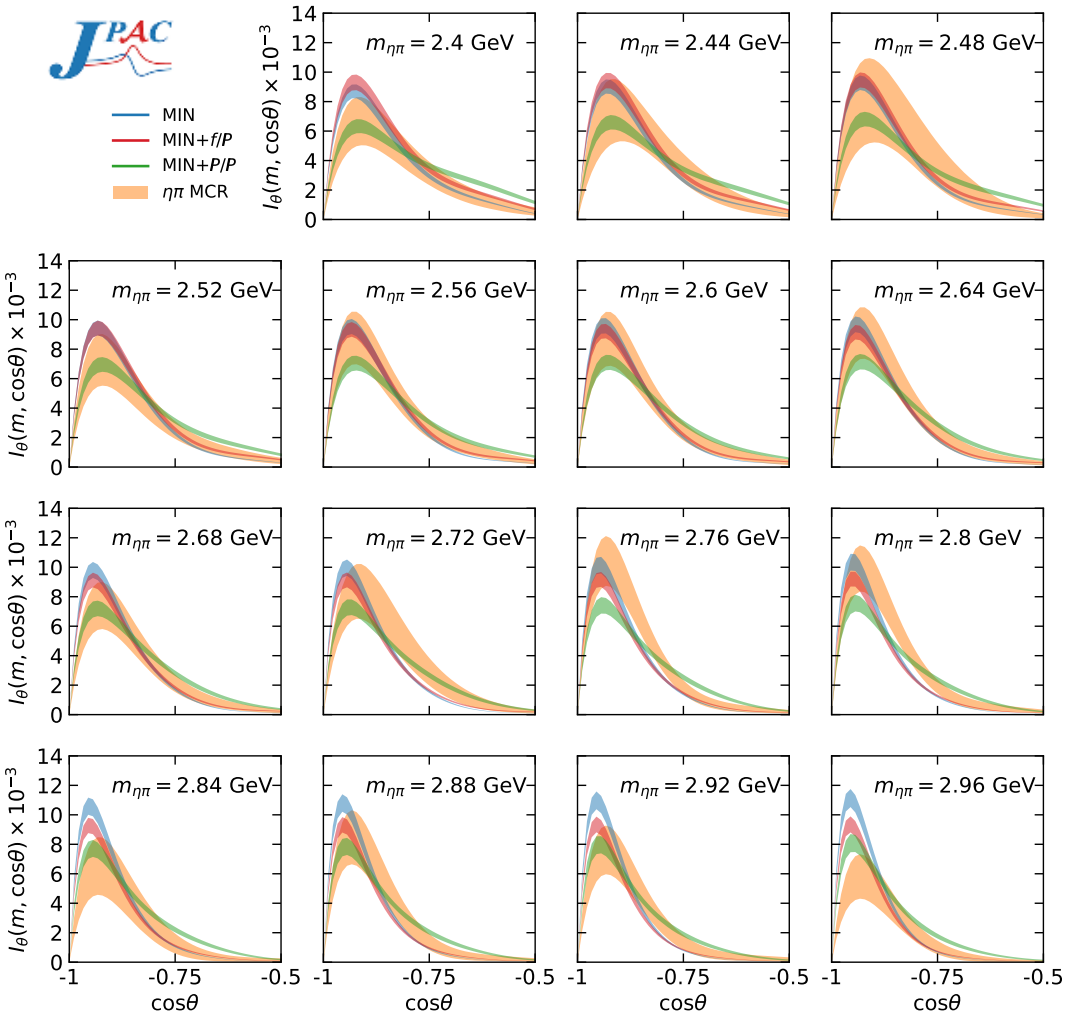

FIG. 13. Same as Fig. 12 for the $\eta\pi$ backward region. Model differences are now apparent.

larger for the MVR than for the MCR, as shown in Fig. 20. The existence of the asymmetry is a consequence of the odd (exotic) partial waves contribution. Taking into account the uncertainties in the partial waves makes the asymmetry less acute, but it is still sizeable and negative for both channels. The asymmetry is larger for the $\eta'\pi$ reaction, making this channel appropriate to search for hybrid candidates [7, 8, 44].

VII. CONSTRAINED PARTIAL WAVE ANALYSIS

As discussed earlier in Section IV, the $\left[f^+_{LM}(m)\right]_{\rm Exp}$ amplitudes extracted by COMPASS are not exactly genuine partial waves. It is rather a parametrization that minimizes the ENLL estimator used to fit the actual event distributions. The ENLL fit makes a finite set of amplitudes reproduce the total intensity. Hence, any contribution from higher partial waves gets redistributed into the set included in the fit. Our model contains an infinite number of partial waves, which leads to a mismatch between the model partial waves and the COMPASS ones. The comparison can still be done if we project the model onto partial waves applying the same constrained procedure implemented by COMPASS. For simplicity, we consider $I_{\rm Th}(m,\Omega)$ of Eq. (7), as obtained from MVR. We follow the conventions in Eq. (2). For each energy bin m_i, we extract the constrained partial waves (cPW) by minimizing the ENLL estimator

$$\mathcal{L}(\{f_i\}) = \int \mathrm{d}\Omega \, \left[I_{\rm cPW}(m_i,\Omega\,|\{f_i\}) - I_{\rm Th}(m_i,\Omega) \log I_{\rm cPW}(m_i,\Omega\,|\{f_i\})\right] , \quad (16)$$

where $I_{\rm cPW}$ is given by

$$I_{\rm cPW}(m_i,\Omega\,|\{f_i\}) = \left| \sum_{L,M} \left[f^+_{LM}(m)\right]_{\rm cPW} \Psi^+_{LM}(\Omega) \right|^2 . \quad (17)$$

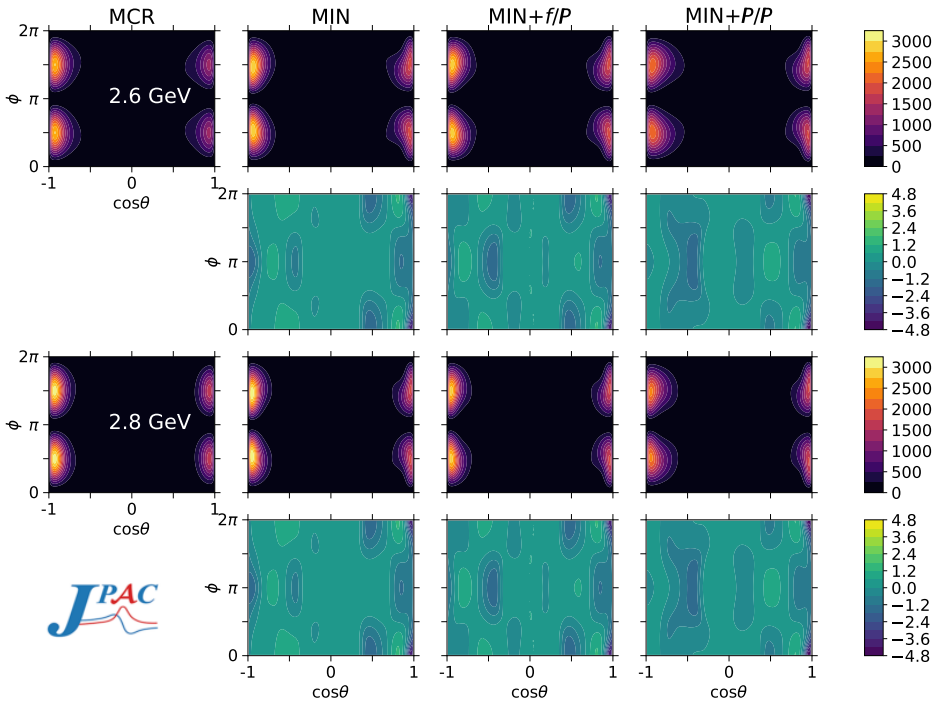

FIG. 14. Examples of $\eta\pi$ density plots for $\bar{I}_{\rm Exp}(m_{\eta\pi},\Omega)$, $\bar{I}_{\rm Th}(m_{\eta\pi},\Omega)$, and $D(m_{\eta\pi},\Omega)$ defined in Eq. (15). The upper two rows displays refer to $m_{\eta\pi}=2.6\,\text{GeV}$, while the lower ones to $m_{\eta\pi}=2.8\,\text{GeV}$. In the second and fourth rows $D(m_{\eta\pi},\Omega)$ shows where the main discrepancies between theory and experiment appear. Most of its structures are located in the small and intermediate $|\cos\theta|$ regions, where the models are expected to be less accurate. Such differences are not large. The largest discrepancies between theory and experiment at the $\cos\theta=1$, $\phi=0,2\pi$ corners. This is a consequence of the exact zero that occurs in both experiment and theory, that makes $D(m_{\eta\pi},\theta,\phi=0)$ indeterminate.

The L,M employed are the same truncated set as COMPASS.

The truncated set of partial waves suffers from the problem of discrete ambiguities, the so-called Barrelet zeros [45]. The intensity $I_{\rm cPW}(m_i,\Omega|\{f_i\})$ with $L=1,\ldots,6$; $M=1$ is identical for 2^5 different sets of parameters $\{f_i\}$, leading to 32 different minima of the $\mathcal{L}(\{f_i\})$ function. These are exact degeneracy for$\eta'\pi$. While the presence of $M=2$ in $\eta\pi$ resolves the exact degeneracy of the solutions. However, these solutions remain as nearly-indistinguishable local minima due to the small size of the $M=2$ components for $\eta\pi$. We select the solution $\{f_i\}$ the closest to the COMPASS $f^+_{LM}(m_i)$ values.

The unconstrained partial waves (uPW) are computed using

$$\left[f^+_{LM}(m)\right]_{\rm uPW}=\sqrt{k(m)}\int \mathrm{d}\Omega\; A_{\rm Th}(m,\Omega)\,\Psi^+_{LM}(\Omega)\,, \tag{18}$$

The cPW, uPW and COMPASS waves are shown in Figs. 21 and 22. As anticipated, the cPW agree with the COMPASS data very well, while the uPW can be quite different. Indeed, the truncation of uPW to the COMPASS set would reduce the integrated intensity to 86% for $\eta\pi$ and 95% for $\eta'\pi$. This is in agreement with the expectations from Figs. 6 and 7, where truncation effects were shown to be critical for $\eta\pi$. The dominant $(2,1)$ intensity in the $\eta\pi$ channel is noteworthy. The unconstrained wave is very small compared to the COMPASS one, but the cPW matches the data, showing how the truncation makes low-lying partial waves to absorb the intensity of higher waves.

VIII. SUMMARY AND CONCLUSIONS

We studied the COMPASS data on the $\pi^-p\to\eta^{(\prime)}\pi^-p$ reactions for $m>2.38\,\text{GeV}$ where the dynamics is expected to be dominated by Regge phenomenology. We considered a double-Regge model composed of up to six amplitudes that account for the possible top/bottom Regge exchanges. In particular, we included $a_2/I\!P$ and a_2/f_2 to describe the fast-η (forward) region, and $f_2/I\!P$, f_2/f_2, $I\!P/I\!P$, $I\!P/f_2$ for the fast-π (backward) region.

The COMPASS collaboration reported partial waves extracted from data under the assumption that only seven (six) partial waves contributed to the $\eta\pi$ ($\eta'\pi$) channel. This is justifiable in the resonance region, *i.e.* $m_{\eta^{(\prime)}\pi}\lesssim 2\,\text{GeV}$. For higher energies, the number of relevant partial waves increases. Our Regge model is not based on a partial wave expansion and therefore implicitly includes all partial waves. Truncating to the set of

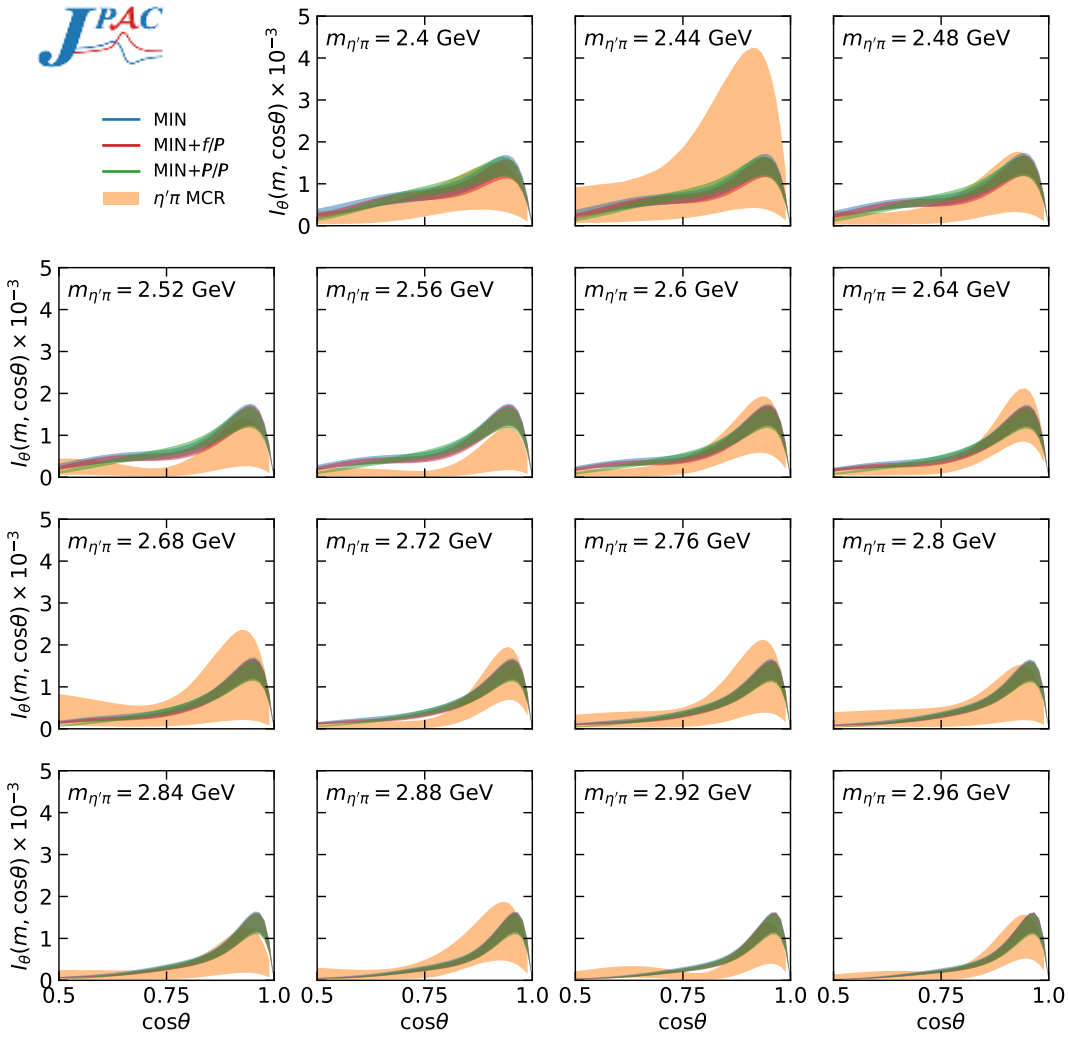

FIG. 15. Same as Fig. 12 for $\eta'\pi$.

waves used by COMPASS is not appropriate for this energy region, as in our model the discarded higher partial waves amount to a nonnegligible contribution to the intensities. Nevertheless, we reconstructed the total intensities from the COMPASS partial waves and fitted with our double-Regge model. We found that the $\eta\pi$ intensity can be well described with four amplitudes, $a_2/I\!P$, a_2/f_2, f_2/f_2, and either $f_2/I\!P$ or $I\!P/I\!P$. The inclusion of either bottom-$I\!P$ amplitude is necessary to describe the forward region, but the data do not show a clear preference for either $f_2/I\!P$ or $I\!P/I\!P$ amplitudes. For this reason, we could not disentangle the contributions from the individual exchanges in the backward direction.

In the $\eta'\pi$ channel, we found that the best model to reproduce the data consists of $a_2/I\!P$, a_2/f_2, f_2/f_2, and $I\!P/I\!P$ amplitudes. The $I\!P/I\!P$ contribution is necessary to describe the data and points to a large gluon affinity of the $\eta'\pi$ system, potentially related to the existence of hybrid mesons. This is also consistent with the observed breakdown of exchange degeneracy between a_2 and f_2 in $\eta'\pi$ production.

The importance of the bottom-f_2 exchange, as shown in the slope of the integrated backward intensity, contradicts the common lore that, at COMPASS energies, the $\eta^{(\prime)}\pi$ pairs are produced via $I\!P$ exchange only, at least for this range of $m_{\eta^{(\prime)}\pi}$.

A consequence of having an amplitude model that contains an infinite number of partial waves is that these cannot match the truncated waves from COMPASS. To bridge this apparent contradiction, we performed a constrained partial wave analysis of the model, using the same procedure as COMPASS. We found that these waves indeed agree well with the COMPASS ones. This proves the importance of studying the full amplitude rather than a truncated partial wave decomposition once the double-Regge regime is reached.

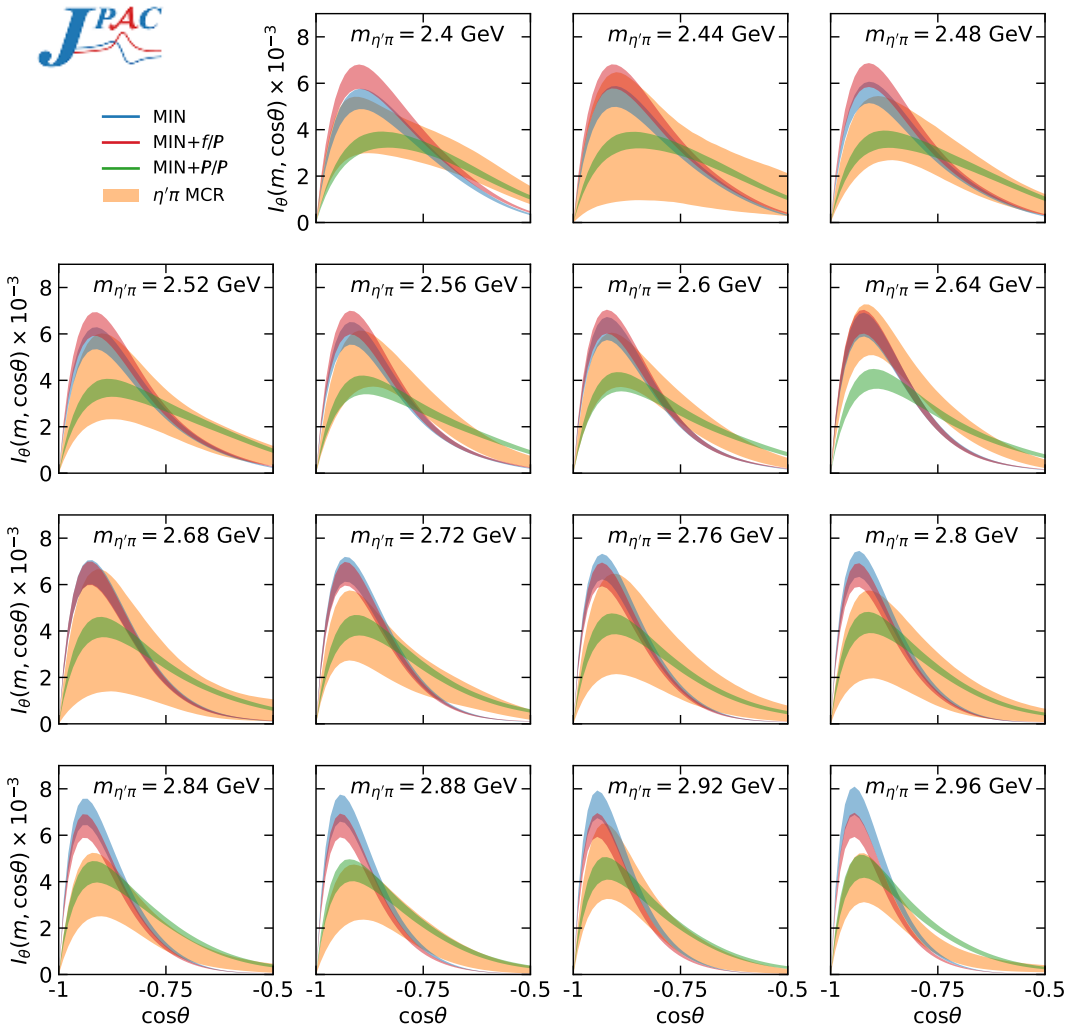

FIG. 16. Same as Fig. 13 for $\eta'\pi$.

ACKNOWLEDGMENTS

We thank COMPASS Collaboration for numerous discussions. Ł.B. acknowledges the financial support and hospitality of Theory Center at Jefferson Lab and the Indiana University. This work was supported by Polish Science Center (NCN) Grant No. 2018/29/B/ST2/02576, PAPIIT-DGAPA (UNAM, Mexico) Grant No. IN106921, CONACYT (Mexico) Grant No. A1-S-21389, Ministerio de Educación, Cultura y Deporte (Spain) Grant No. PID2019-106080GB-C21, and U.S. Department of Energy Grants No. DE-AC05-06OR23177 and No. DE-FG02-87ER40365. V.M. is a Serra Húnter fellow and acknowledges support from the Community of Madrid through the Programa de Atracción de Talento Investigador 2018-T1/TIC-10313. A.P. has received funding from the European Union's Horizon 2020 research and innovation programme under the Marie Skłodowska-Curie grant agreement No. 754496.

Appendix A: Kinematics

The momenta of the reaction in Eq. (1) in the GJ frame are represented in Fig. 23. In this frame,

$$q = (E_q, \mathbf{q})\,, \qquad p_{1,2} = (E_{1,2}, \mathbf{p}_{1,2})\,, \tag{A1a}$$

$$k_\eta = (E_\eta, \mathbf{k})\,, \qquad k_\pi = (E_\pi, -\mathbf{k})\,. \tag{A1b}$$

In the $\eta\pi$ center-of-mass, the $\hat{z}$-axis is along the beam and the $\hat{y}$-axis, perpendicular to the production plane, is parallel to $\mathbf{q} \times \mathbf{p_2}$.

The particle energies can be expressed in terms of in-

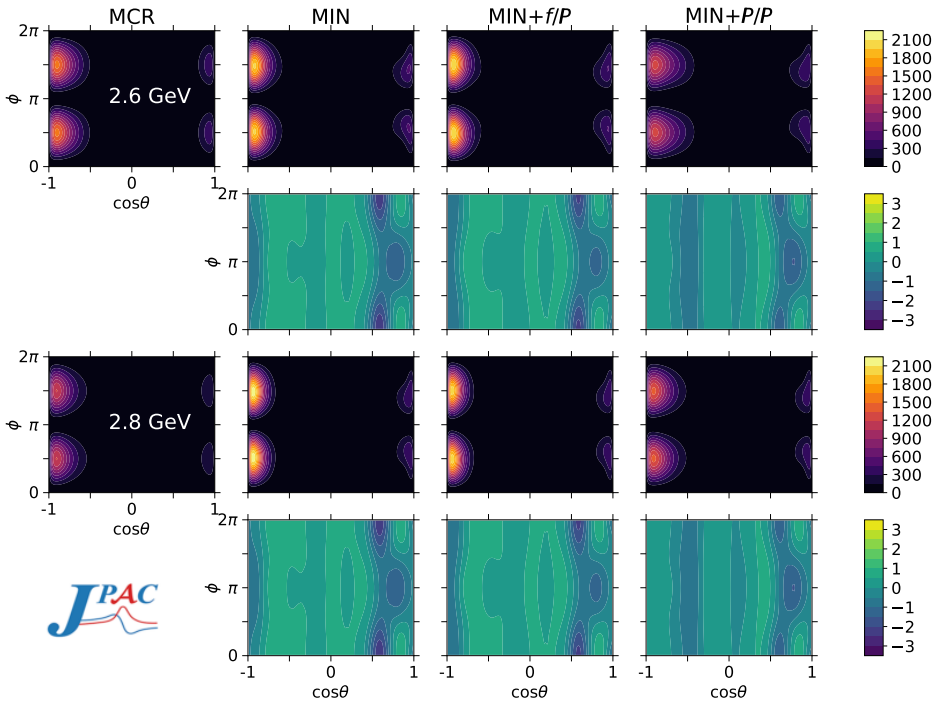

FIG. 17. Same as Fig. 14 for the $\eta'\pi$ channel.

variants as

$$E_q = (m_{\eta\pi}^2 - t_p + m_\pi^2)/2m_{\eta\pi}, \tag{A2a}$$
$$E_1 = (s - m_p^2 + t_p - m_\pi^2)/2m_{\eta\pi}, \tag{A2b}$$
$$E_2 = (s - s_{\eta\pi} - m_p^2)/2m_{\eta\pi}, \tag{A2c}$$
$$E_\pi = (m_{\eta\pi}^2 + m_\pi^2 - m_\eta^2)/2m_{\eta\pi}, \tag{A2d}$$
$$E_\eta = (m_{\eta\pi}^2 + m_\eta^2 - m_\pi^2)/2m_{\eta\pi}. \tag{A2e}$$

ξ and ϵ are the angles between the beam and the target, and between the beam and the recoil, respectively. They are given by

$$2|\mathbf{q}||\mathbf{p}_1|\cos\xi = s - 2\,E_q\,E_1 - m_p^2 - m_\pi^2\,, \tag{A3a}$$
$$2|\mathbf{q}||\mathbf{p}_2|\cos\epsilon = s - 2\,E_q\,E_2 - m_p^2 - m_{\eta\pi}^2 + t_p\,, \tag{A3b}$$

where t_η and $s_{\pi p}$ are defined in Eq. (8a). The energies and the nucleon angles depend only on s, $m_{\eta\pi}^2$ and t_p. The polar and azimuthal angles of the η must then depend on the remaining independent invariants. Indeed we obtain

$$t_\eta = m_\pi^2 + m_\eta^2 - 2E_qE_\eta + 2|\mathbf{q}||\mathbf{k}|\cos\theta\,, \tag{A4a}$$
$$s_{\pi p} = m_\pi^2 + m_p^2 + 2E_2E_\pi - 2|\mathbf{p}_2||\mathbf{k}|\,(\sin\epsilon\sin\theta\cos\phi + \cos\epsilon\cos\theta)\,. \tag{A4b}$$

The invariants t_π and $s_{\eta p}$ needed in fast-π amplitudes and defined in Eq. (8b) are related to the other Mandelstam variables by

$$s_{\eta p} = s - s_{\pi p} - m_{\eta\pi}^2 + m_\eta^2 + m_\pi^2 + m_p^2, \tag{A5a}$$
$$t_\pi = t_p - t_\eta - m_{\eta\pi}^2 + m_\eta^2 + 2m_\pi^2. \tag{A5b}$$

The kinematic function K that appears in Eq. (9) is given by

$$K = \varepsilon_{\alpha\beta\gamma\delta}(q+p_2)^\alpha(q-p_2)^\beta(k_\eta+k_\pi)^\gamma(k_\eta-k_\pi)^\delta = 4m_{\eta\pi}|\mathbf{q}||\mathbf{k}||\mathbf{p}_2|\sin\epsilon\sin\theta\sin\phi\,. \tag{A6}$$

Appendix B: MCR and bootstrap

We describe how the MCR is performed, and consequently the bootstrap fit to it. The first step is to associate a probability distribution with each intensity and phase shift and, then, to resample the distributions N times (in our case $N = 10^4$) to achieve enough precision in the extracted distributions. If uncertainties are only of statistical origin, the uncertainty in percentage can be computed as $\pm\sqrt{N}/N \times 100\%$, which for $N = 10^4$ is $\pm1\%$, *i.e.* a total 2% uncertainty. For each resampling we can compute the value of a given observable, namely $I(m,\Omega)$, $I_\theta(m,\cos\theta)$, $F(m)$, $B(m)$, $T(m)$, and $A(m)$, and we can fit the pseudodataset obtaining the corresponding parameters $\{c\}$ (bootstrap fit) [46–48]. Then, the expected value (mean) of each observable and the associated uncertainty (16% and 84% quantiles to obtain the 68% error bands) can be computed. Equivalently for the $\{c\}$ distributions and any observable computed for them. For the intensities, we associate to each data point a Gaussian distribution

$$f(x|\mu,\sigma) = \frac{1}{\sqrt{2\pi}\,\sigma}\mathrm{e}^{-\frac{1}{2}\left(\frac{x-\mu}{\sigma}\right)^2}\,, \tag{B1}$$

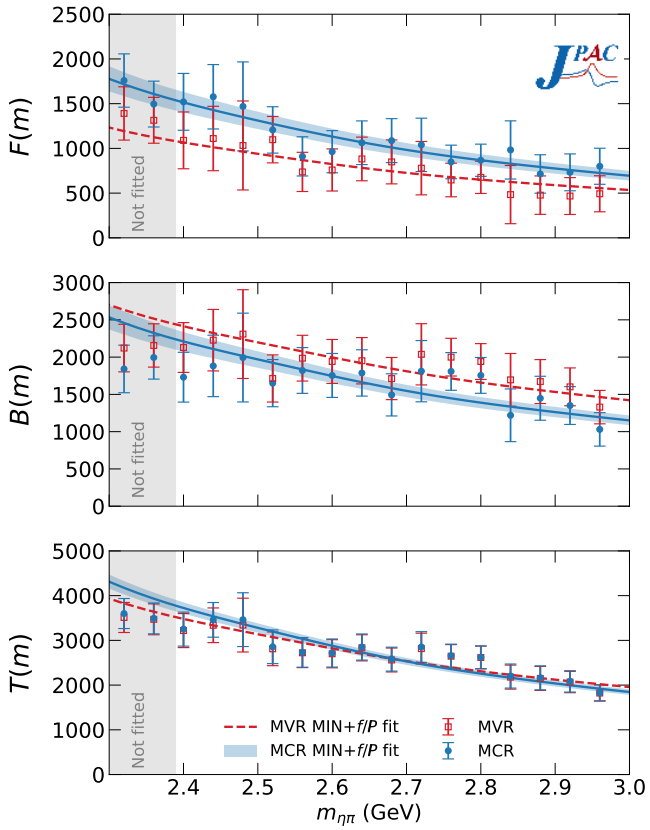

FIG. 18. Forward (upper), backward (center), and total (lower) intensities for the $\eta\pi$ channel as defined in Eq. (5) for the MCR and MVR and their respective MIN+$f/I\!P$ fits.

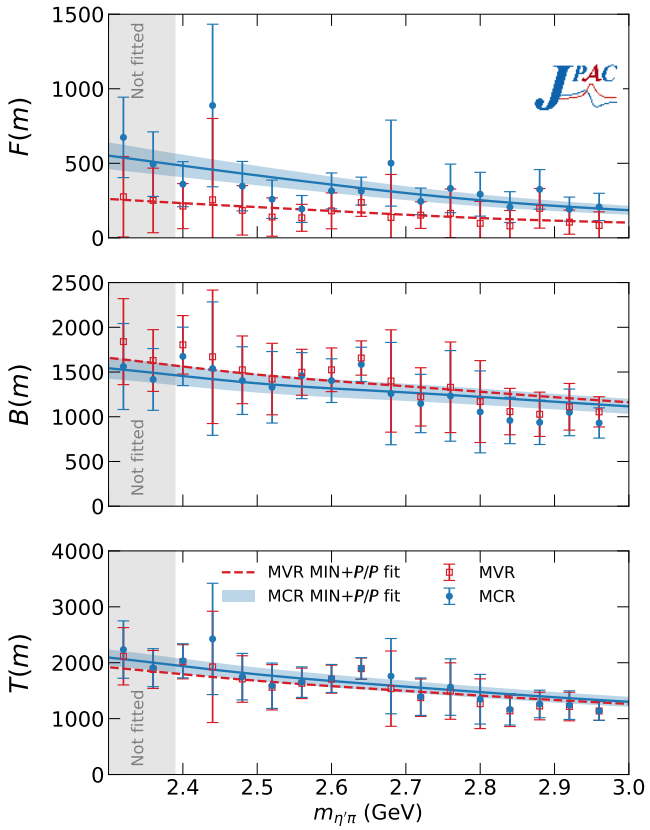

FIG. 19. Same as Fig. 18 for the $\eta'\pi$ data and the MIN+$I\!P/I\!P$ model.

with μ equal to the mean value reported by COMPASS, and σ equal to the uncertainty. Hence, we assume that the uncertainties are statistical only, that all intensities within a given partial wave are statistically independent, and that the partial waves are uncorrelated. This is not a true assumption but a necessary one given that the correlation information is not available from the COMPASS analysis. This assumption leads to an overestimation of the error bands. There is an additional caveat: some of the uncertainties are large enough to make the intensities negative, which is unphysical. Hence, if a resampling provides a negative intensity for a given m, we set that particular intensity to zero. We checked the impact of this choice by taking the absolute value of the intensity and subtracting it in Eq. (2) instead of setting the value to zero. We found the effect to be negligible in the resulting MCR distributions and fits. For the phase shifts, we use the $[-\pi, \pi]$ periodic equivalent to the Gaussian distribution, *i.e.* the von Mises distribution

$$f(x|\mu,\kappa) = \frac{1}{2\pi I_0(\hat{\kappa})} \mathrm{e}^{\kappa\cos(x-\mu)}\,, \qquad \text{(B2)}$$

where $I_0(\hat{\kappa})$ is the modified Bessel function of order 0. The μ parameter is equivalent to the mean in a Gaussian distribution and we set it to the mean value of each phase shift. The concentration parameter $\hat{\kappa}$ is the reciprocal measurement of the dispersion. Hence $1/\hat{\kappa}$ is analogous to σ^2 in a Gaussian distribution and has to be determined. If the phase shift uncertainty is small, the Gaussian distribution with σ equal to the experimental uncertainty is almost equal to the von Mises distribution with $\hat{\kappa} = 1/\sigma^2$ as shown in the upper plot in Fig. 24. However, for larger values of the uncertainty, the Gaussian and the von Mises distributions are quite different. In the lower plot in Fig. 24 we compare for a phase shift of 0 ± 96.59^o (this uncertainty value corresponds to one of the largest in the COMPASS phase shifts) the following three cases: (i) Gaussian distribution with $\mu = 0$ and $\sigma = 96.59\pi/180$; (ii) von Mises distribution with $\mu = 0$ and $\hat{\kappa} = 1/\sigma^2$; and (iii) von Mises distribution with $\mu = 0$ and $\hat{\kappa} = 0.56$ given by a fit to the Gaussian distribution in (i). In this third scenario we build the closest von Mises distribution to the Gaussian that would be associated with the COMPASS phase shift and uncertainty. The grey bands in Fig. 24 provide the region outside the $[-\pi, \pi]$ range and highlight how the Gaussian distribution would be inappropriate to describe a periodic phase shift. For small phase shift uncertainties (which we set to be $\leq$ 16 degrees) we use option (ii) as both Gaussian and von Mises are essentially equal, while for larger uncertainties we prefer option (iii). The reason is that

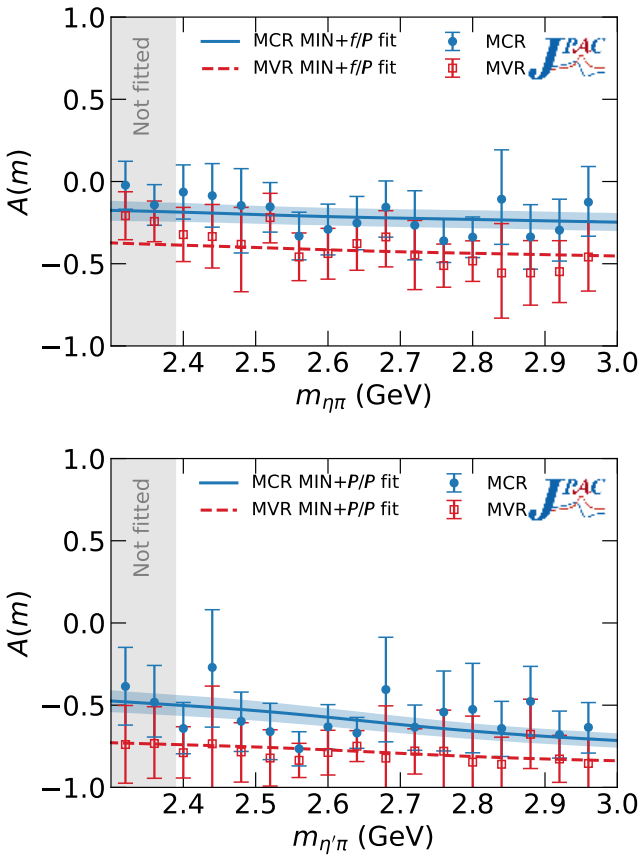

FIG. 20. Forward-backward intensity asymmetry as defined in Eq. (5) for $\eta\pi$ (upper) and $\eta'\pi$ (lower) for both MCR and MVR.

option (iii) is closer to the spread expectation from a Gaussian distribution, and hence, we believe convenes a better description of the actual experimental uncertainties. Nevertheless, we computed the MCR with the three options for the phase shifts distributions and we did not find a relevant difference among the results.

Appendix C: MVR vs. MCR observables

In Section II we mentioned that there were meaningful differences between the MVR and MCR. These differences are highlighted in the $I_\theta(m, \cos\theta)$ distributions, Eq. (4), the forward $F(m)$ and backward $B(m)$ intensities, and the forward-backward asymmetry $A(m)$, Eq. (5). In particular, for $I_\theta(m, \cos\theta)$ the fast-η peak is smaller for the MVR than for the MCR. This can be noticed in both Fig. 1 for the $\eta\pi$ channel and in Fig. 2 for the $\eta'\pi$. It can also be noticed in the integrated forward intensity of Figs. 18 and 19, where $F(m)$ is systematically larger for the MCR. The opposite is true for the fast-π peak and $B(m)$, which are systematically larger for the MVR. Consequently, the forward-backward asymmetry $A(m)$, defined in Eq. (5c), is, in absolute value, larger for the MVR than for the MCR, as shown in Fig. 20. The total intensity $T(m)$ is very similar for both MCR and MVR, as displayed in Fig. 4.

The difference between MVR and MCR is also apparent if we inspect the small $|\cos\theta|$ region for the $I_\theta(m, \cos\theta)$ observable. The inclusion of the uncertainties and the calculation of expected values in the MCR leads to a smearing that flattens the experimental distribution. This effect is shown in Fig. 25. The double-Regge approximation is designed to describe the fast-π and fast-η regions, and hence is not reliable in the small $|\cos\theta|$ region. Consequently, the fits to the MVR present the problem that they try to match structures that are mostly wiped out by the uncertainties. Hence, the fits to the MVR are more sensitive to details in the small angle region. Removing the small $|\cos\theta|$ region from the fits is not feasible given that the total intensity is an important experimental constraint. Consequently, we consider the physics extracted from the MCR fits more reliable.

Appendix D: Statistical analyses of the likelihood

As mentioned in Section VI B, because of the continuous nature of the angular variables and the fact that $\mathcal{L}$ is constructed to match the experimental total intensity, we cannot compare models with a different number of parameters. However, we can compare fits with the same number of parameters such as MIN+$f/\mathbb{P}$ and MIN+$\mathbb{P}/\mathbb{P}$. In Table Iwe saw that the MIN+$\mathbb{P}/\mathbb{P}$ fit was slightly better than the MIN+$f/\mathbb{P}$ for both $\mathcal{L}_{\rm MVR}$ and $\mathcal{L}_{\rm MCR}$, although it did not look significant enough. The comparison between the two models can be formalized by checking if, for any given resampling of the intensities and phase shifts, one of the models is systematically better. In doing so, we build 10^3 resampled datasets for each channel and we fit each dataset j with both models. Then we compute the difference between the two ENLL

$$\Delta\mathcal{L}_j = \mathcal{L}_j(\text{MIN} + f/\mathbb{P}) - \mathcal{L}_j(\text{MIN} + \mathbb{P}/\mathbb{P})\,. \quad \text{(D1)}$$

Figure 26 shows the result of this exercise. We find that for $\eta'\pi$ (lower plot), $\mathcal{L}_{\rm MCR}$ for the MIN+$\mathbb{P}/\mathbb{P}$ fits is not only better on *average* than the MIN+$f/\mathbb{P}$ fits as shown in Table Iand Fig. 11, but that it is better systematically and significantly for any given resampling of the COMPASS intensities and phase shifts. This leads us to prefer the MIN+$\mathbb{P}/\mathbb{P}$ for the $\eta'\pi$ channel.

For $\eta\pi$ we also find that the MIN+$\mathbb{P}/\mathbb{P}$ model is slightly better, although the result is not as appealing as in the $\eta'\pi$ case. For 96.5% of the resampled datasets[3] the MIN+$\mathbb{P}/\mathbb{P}$ is preferred, and the $\Delta\mathcal{L}_j$ average is not that large. Hence, there is a slight preference for the MIN+$\mathbb{P}/\mathbb{P}$ model, but we show in Section VI B 1 that this preference is not conclusive.

[3] We note that the uncertainty in the percentage is expected to be approximately $\pm\sqrt{N}/N \times 100\%$, which for $N = 10^3$ is $\pm 3.2\%$.

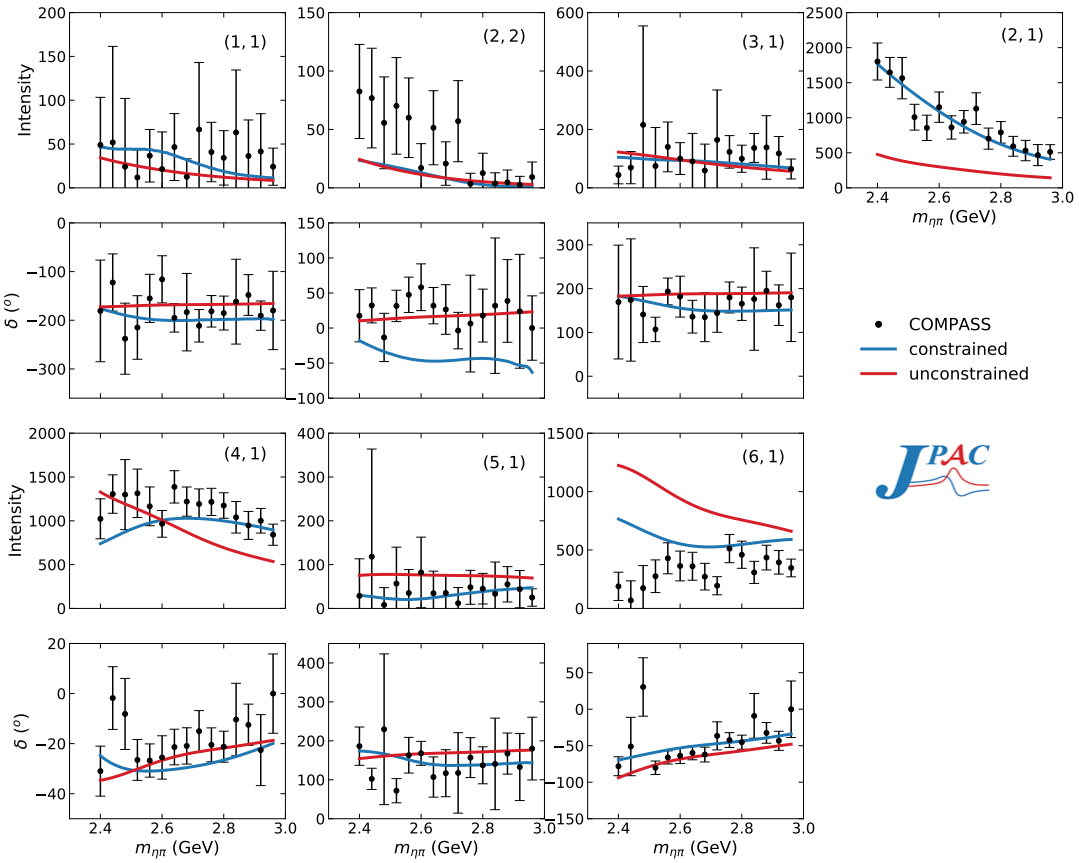

FIG. 21. Constrained (red) and unconstrained (blue) $\eta\pi$ partial waves from Eqs. (18) and (16) for the MIN+$f_2/I\!P$, compared with the COMPASS data (black) . Partial waves intensities are labeled as (L, M) and the corresponding phases δ are presented below them. In this convention, $\delta_{21} \equiv 0$.

Appendix E: MVR fits

The fit parameters to the MVR for the three models in both channels are presented in the MVR columns of Table I. No error is provided as none can be reliably computed.

For the fast-η amplitudes, *i.e.* $a_2/I\!P$ and a_2/f_2, we find that the $c_{a_2 I\!P}$ and $c_{a_2 f_2}$ parameters are similar for the three models. This is not unexpected, as for the forward peak all three models are the same and the correlation between forward and backward peaks has to be very small. The largest difference between the top-a_2 parameters appears when comparing the MIN+$I\!P/I\!P$ model to MIN and MIN+$f/I\!P$, particularly in the $\eta'\pi$ channel. This is due to the wider nature of the $I\!P/I\!P$ amplitude (see Figs. 6 and 7) in the $\cos\theta$ variable, interfering with the top-a_2 amplitudes in the central region. However, our double-Regge model is based on the leading Regge poles and describes best the physics at small scattering angles, not in the central region where corrections (cuts and daughters) are expected. Hence, any correlation or interplay among the amplitudes in the central region cannot be trusted.

The fast-π f_2/f_2 amplitude is common to the three models. If $SU(3)$ symmetry were realized we should obtain $c_{a_2 f_2} = -c_{f_2 f_2}$. Our result shows that $SU(3)$ symmetry is broken for both channels, with larger breaking for η' than for η, regardless of the inclusion of additional amplitudes such as $I\!P/I\!P$ or $f_2/I\!P$. The $c_{f_2 f_2}$ parameter is larger for the MIN fit than for either MIN+$f_2/I\!P$ or MIN+$I\!P/I\!P$. The reason is that the total intensity is a constraint in the fit, and in the MIN fit the forward intensity has to be matched only by the f_2/f_2 amplitude, while for the other two fits it is distributed between two amplitudes instead of one. Further comparison among the parameters is meaningless due to the lack of uncertainties.

1. MVR vs. MCR fits

The differences between the MVR and the MCR fits show up in the fitted parameters displayed in Table I. Let us compare MVR and MCR parameters using the MVR ones as reference. For the $\eta\pi$ channel we notice that the $c_{a_2 I\!P}$ parameter, $a_2/I\!P$ amplitude, is larger for the MCR while the $c_{a_2 f_2}$, a_2/f_2 amplitude, is very similar for both MVR and MCR fits. This happens for all of the

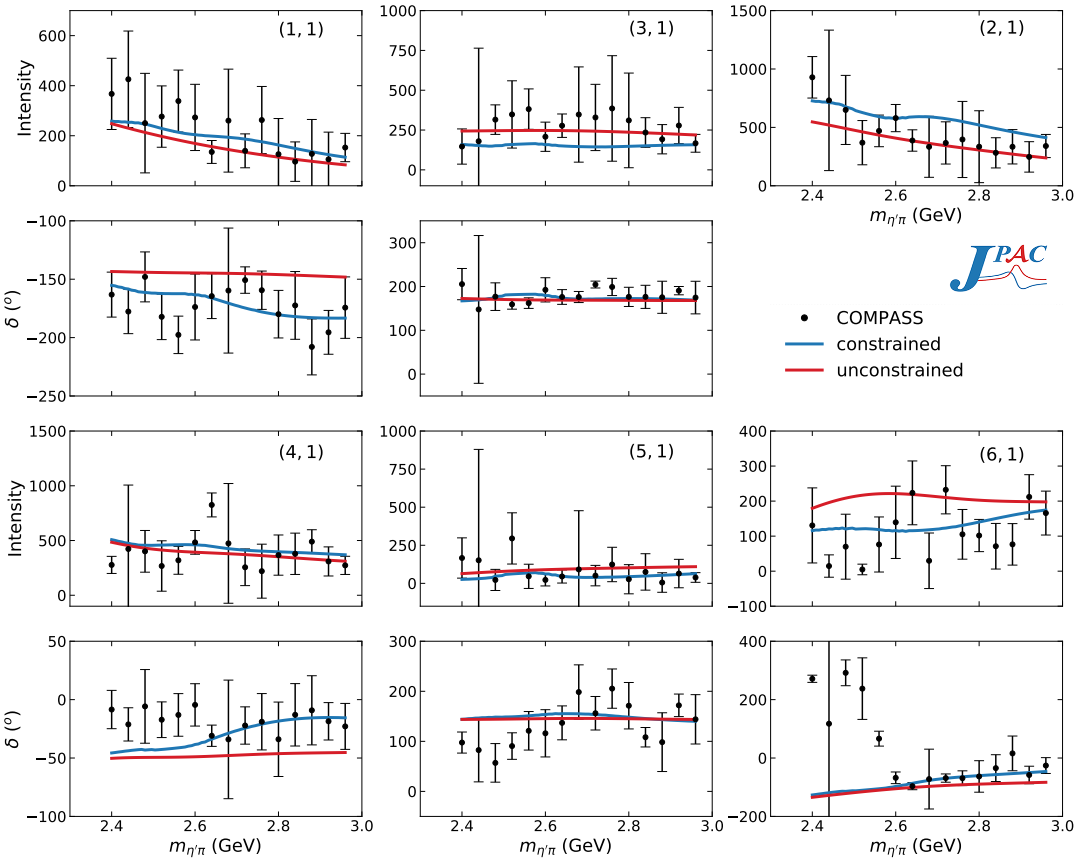

FIG. 22. Same as Fig. 21 for the $\eta'\pi$ system and the MIN+$I\!P/I\!P$ fit.

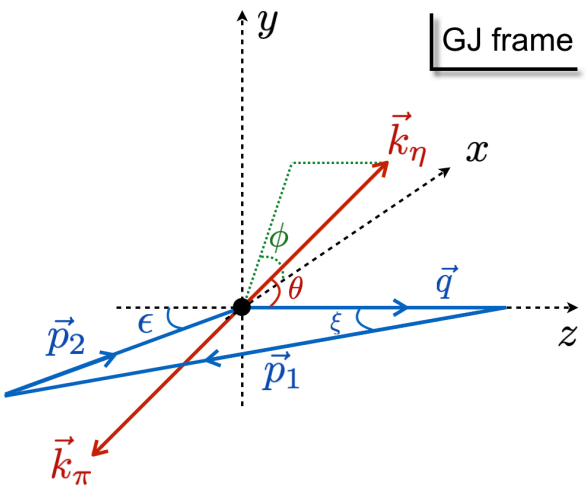

FIG. 23. GJ reference frame. See text in Appendix A for the definition of the variables and vectors.

MIN, MIN+$f/I\!P$, and MIN+$I\!P/I\!P$ models and it means that the extra strength in the MCR is embedded in the $a_2/I\!P$ contribution while the a_2/f_2 stays the same. For the $\eta'\pi$ channel we find the same behavior for $c_{a_2 I\!P}$, *i.e.* it is larger for the MCR fits and very similar for all the models. However, the $c_{a_2 f_2}$ parameter value is very different for the MVR and the MCR fits. For the MCR, the three models provide similar results, within uncertainties. Moreover, the a_2/f_2 exchange is compatible with zero for the three models within a 2σ confidence level (1σ for MIN), signaling a large EXD breaking. For the MVR fits, the a_2/f_2 amplitude is larger than for the MCR and yields very similar results for the MIN and MIN+$f/I\!P$ models. The MIN+$I\!P/I\!P$ $c_{a_2 f_2}$ is not very dissimilar to the other two models, but clearly smaller. This is due to the non-negligible interference between the top-a_2 amplitudes and the $I\!P/I\!P$ contribution. Hence, MVR and MCR fits provide a very different balance between the two fast-η amplitudes. For the fast-π region, we find that the $c_{f_2 f_2}$ parameter is larger for the MVR fits than for the MCR ones for both channels, as expected. Regarding the asymmetry, for both $\eta\pi$ and $\eta'\pi$ channels it is negative, as shown in Fig. 20. Taking into account the uncertainties in the partial waves makes the asymmetry less acute, but it is still sizeable.

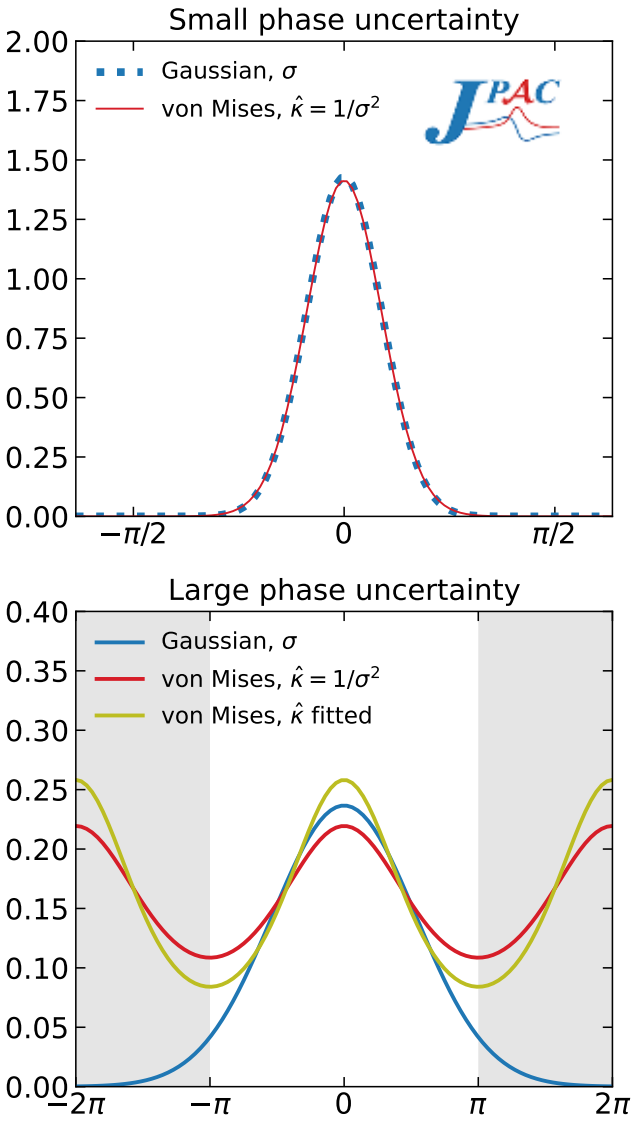

FIG. 24. Comparison between the Gaussian and von Mises distributions for small (top) and large (bottom) phase shift uncertainties. The grey bands provide the region outside the $[-\pi, \pi]$ range.

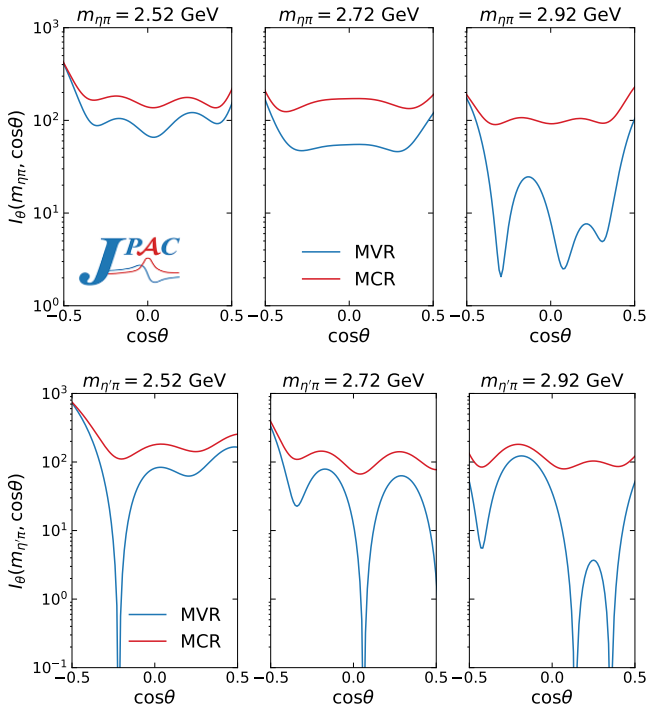

FIG. 25. MCR (red) vs. MVR (blue) for the $I_\theta(m_{\eta\pi}, \cos\theta)$ observable in the $\eta\pi$ (top) and $\eta'\pi$ (bottom) channels and the small $\cos\theta$ region, $-0.5 \leq \cos\theta \leq 0.5$, for three $m_{\eta\pi}$ energies.

Appendix F: Parameter distributions and correlations

The bootstrap fits to the MCR provide the parameter distributions and their correlations. We show the correlation matrices in Fig. 27 and the fit parameter distributions in Fig. 28 for both MIN+$f/I\!P$ and MIN+$I\!P/I\!P$ fits to both channels. We do not show the results for the MIN fits as they were discarded in Sections VI B 1 and VI B 2 as an appropriate description of the $I(m, \Omega)$ distributions.

From the correlation matrices the independence between fast-π and fast-η amplitudes is apparent for both models and channels. A certain unavoidable correlation is present because of the fixed total intensity constraint and the overlap in the small $|\cos\theta|$ region, but both regions can be regarded as mostly independent.

For the $\eta\pi$ channel, the parameters for the MIN+$f/I\!P$ model are well determined and display a Gaussian behavior. However, this does not happen for the MIN+$I\!P/I\!P$ model, where the $I\!P/I\!P$ amplitude parameter is not well determined and presents a bimodal distribution. The fit to the MVR using the MIN+$I\!P/I\!P$ model presents a single and isolated absolute minimum, so the appearance of a two peak structure in the fit to the MCR is entirely due to the inclusion of the uncertainties, and the $I\!P/I\!P$ amplitude parameter $c_{I\!P\,I\!P}$ cannot be well determined. The parameter distributions for $a_2/I\!P$ and a_2/f_2 for both MIN+$f/I\!P$ (red) and MIN+$I\!P/I\!P$ (green) mostly overlap. For f_2/f_2, the MIN+$f/I\!P$ and MIN+$I\!P/I\!P$ distributions barely overlap, as a consequence of the differences between the $f_2/I\!P$ and $I\!P/I\!P$ amplitudes.

For the $\eta'\pi$ channel, all the parameters for both models are well determined and display a Gaussian behavior. The $c_{a_2 f_2}$ distribution is compatible with zero at a 2σ level for both models, indicating that it is possible that the associated amplitude vanishes. This would mean a large violation of the EXD between the a_2 and f_2 Regge poles. Given that both the statistical analysis in Appendix D and the comparison to the data in Section VI B 2 favor the MIN+$I\!P/I\!P$, we find that the contribution of all four amplitudes ($a_2/I\!P$, a_2/f_2, f_2/f_2, and $I\!P/I\!P$) to the $\eta'\pi$ process can be well established

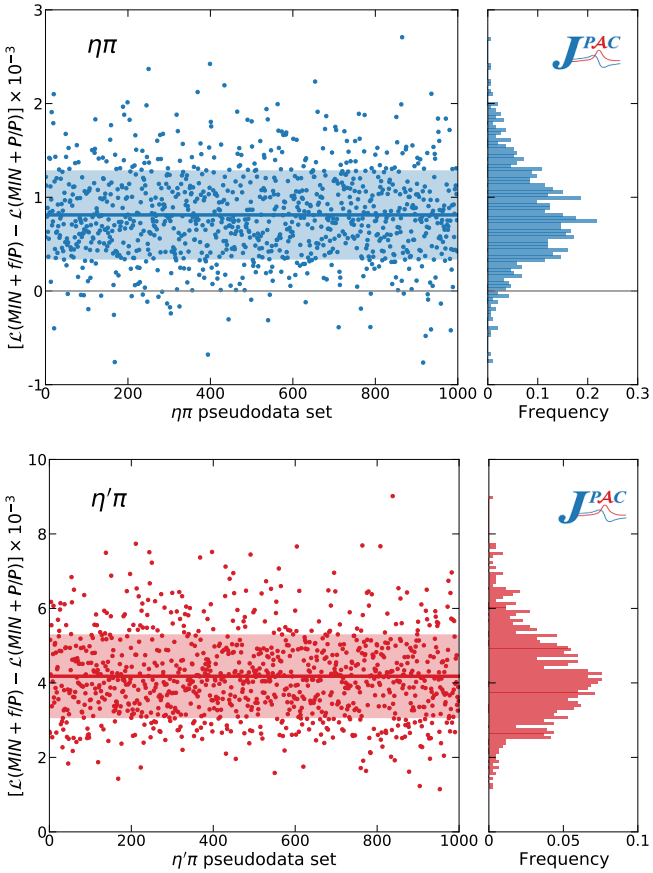

FIG. 26. Extended negative log-likelihood difference $\Delta\mathcal{L}_j$ for 10^3 MCR $\eta\pi$ (upper, red) and 10^3 MCR $\eta'\pi$ (lower, green) resamples. For each MCR resampled dataset we perform both MIN+$f/\mathbb{P}$ and MIN+$\mathbb{P}/\mathbb{P}$ and compute the difference. The right plots provide the density distributions for the $\Delta\mathcal{L}_j$. The red (green) line is the mean of the distribution and the band represents the 68% confidence level. The grey line in the upper plot marks the zero value of the $\Delta\mathcal{L}_j$.

within reasonable uncertainties.

[1] M. R. Shepherd, J. J. Dudek, and R. E. Mitchell, Nature **534**, 487 (2016).
[2] E. Klempt and A. Zaitsev, Phys.Rept. **454**, 1 (2007), arXiv:0708.4016 [hep-ph].
[3] F.-K. Guo, C. Hanhart, U.-G. Meißner, Q. Wang, Q. Zhao, and B.-S. Zou, Rev.Mod.Phys. **90**, 015004 (2018), arXiv:1705.00141 [hep-ph].
[4] A. Esposito, A. Pilloni, and A. D. Polosa, Phys.Rept. **668**, 1 (2017), arXiv:1611.07920 [hep-ph].
[5] S. L. Olsen, T. Skwarnicki, and D. Zieminska, Rev.Mod.Phys. **90**, 015003 (2018), arXiv:1708.04012 [hep-ph].
[6] M. Karliner, J. L. Rosner, and T. Skwarnicki, Ann.Rev.Nucl.Part.Sci **68**, 10.1146/annurev-nucl-101917-020902 (2018), arXiv:1711.10626 [hep-ph].
[7] J. J. Dudek, Phys.Rev. **D84**, 074023 (2011), arXiv:1106.5515 [hep-ph].
[8] C. A. Meyer and E. S. Swanson, Prog.Part.Nucl.Phys. **82**, 21 (2015), arXiv:1502.07276 [hep-ph].
[9] C. Adolph *et al.* (COMPASS), Phys.Lett. **B740**, 303 (2015), arXiv:1408.4286 [hep-ex].
[10] A. Rodas *et al.* (JPAC), Phys.Rev.Lett. **122**, 042002 (2019), arXiv:1810.04171 [hep-ph].
[11] B. Kopf, M. Albrecht, H. Koch, J. Pychy, X. Qin, and U. Wiedner, arXiv:2008.11566 [hep-ph] (2020).
[12] A. J. Woss, J. J. Dudek, R. G. Edwards, C. E. Thomas, and D. J. Wilson, arXiv:2009.10034 [hep-lat] (2020).
[13] R. Dolen, D. Horn, and C. Schmid, Phys.Rev. **166**, 1768 (1968).
[14] R. Dolen, D. Horn, and C. Schmid, Phys.Rev.Lett. **19**, 402 (1967).
[15] R. Brower, C. E. DeTar, and J. Weis, Phys.Rept. **14**, 257 (1974).
[16] A. Austregesilo (GlueX), Int.J.Mod.Phys.Conf.Ser. **46**, 1860029 (2018), arXiv:1801.05332 [nucl-ex].
[17] C. Gleason (GlueX), in *18th International Confer-*

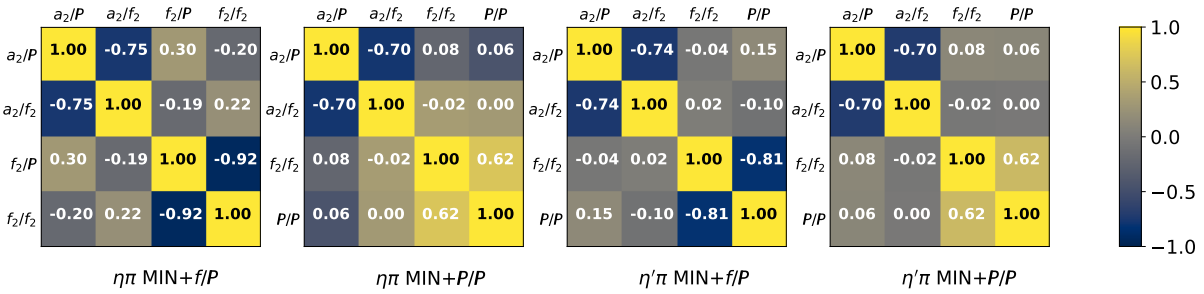

FIG. 27. Correlation plots for the fit parameters of the MIN+$f/\mathbb{P}$ and MIN+$\mathbb{P}/\mathbb{P}$ models for both $\eta\pi$ and $\eta'\pi$ channels.

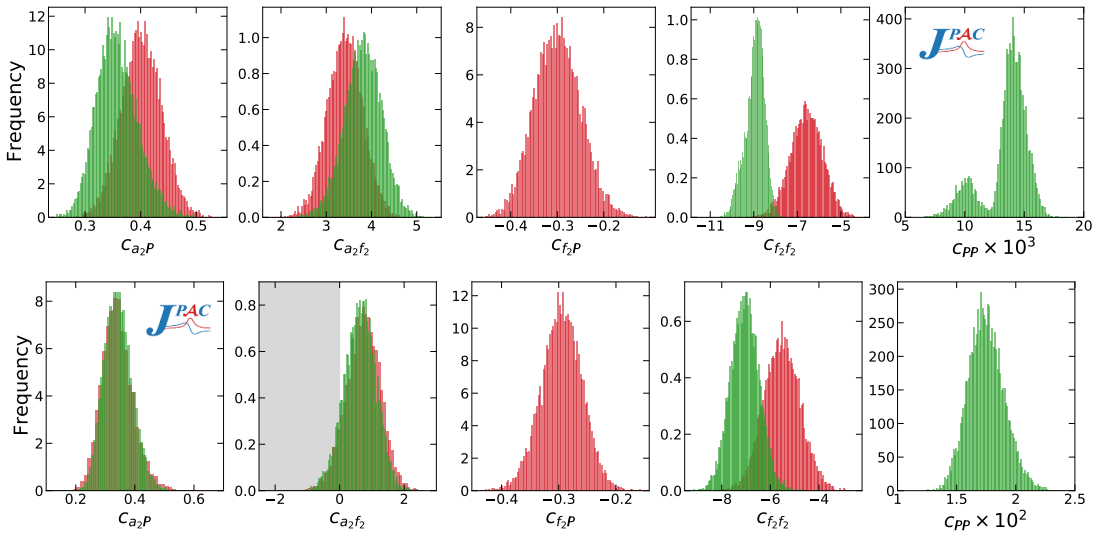

FIG. 28. $\eta\pi$ (top row) and $\eta'\pi$ (bottom row) MCR fit parameter distributions for the MIN+$f/\mathbb{P}$ (red) and the MIN+$\mathbb{P}/\mathbb{P}$ (green) models. The grey area highlights the region where $c_{a_2f_2}$ is negative.

ence on Hadron Spectroscopy and Structure (2020) arXiv:2001.05404 [nucl-ex].

[18] B. Ketzer, B. Grube, and D. Ryabchikov, Prog.Part.Nucl.Phys. **113**, 103755 (2019), arXiv:1909.06366 [hep-ex].

[19] V. Mathieu, M. Albaladejo, C. Fernández-Ramírez, A. Jackura, M. Mikhasenko, A. Pilloni, and A. Szczepaniak (JPAC), Phys.Rev. **D100**, 054017 (2019), arXiv:1906.04841 [hep-ph].

[20] L. Lyons and W. Allison, Nucl.Instrum.Meth. **A245**, 530 (1986).

[21] R. J. Barlow, Nucl.Instrum.Meth. **A297**, 496 (1990).

[22] F. James, *Statistical methods in experimental physics* (2006).

[23] A. Schwimmer, Phys.Rev. **184**, 1508 (1969).

[24] I. Drummond, P. Landshoff, and W. Zakrzewski, Nucl.Phys. **B11**, 383 (1969).

[25] N. F. Bali, G. F. Chew, and A. Pignotti, Phys.Rev.Lett. **19**, 614 (1967).

[26] I. Drummond, P. Landshoff, and W. Zakrzewski, Phys.Lett. **B28**, 676 (1969).

[27] J. Weis, Phys.Rev. **D6**, 2823 (1972).

[28] P. D. B. Collins, *An Introduction to Regge Theory and High-Energy Physics*, Cambridge Monographs on Mathematical Physics (Cambridge Univ. Press, Cambridge, UK, 2009).

[29] T. Shimada, A. D. Martin, and A. C. Irving, Nucl.Phys. **B142**, 344 (1978).

[30] P. Lebiedowicz, O. Nachtmann, and A. Szczurek, Phys.Rev. **D99**, 094034 (2019), arXiv:1901.11490 [hep-ph].

[31] P. Lebiedowicz, J. Leutgeb, O. Nachtmann, A. Rebhan, and A. Szczurek, Phys.Rev. **D102**, 114003 (2020), arXiv:2008.07452 [hep-ph].

[32] A. Cisek and A. Szczurek, arXiv:2103.08954 [hep-ph] (2021).

[33] V. Mathieu, G. Fox, and A. P. Szczepaniak, Phys.Rev. **D92**, 074013 (2015), arXiv:1505.02321 [hep-ph].

[34] V. Mathieu, I. V. Danilkin, C. Fernández-Ramírez, M. R. Pennington, D. Schott, A. P. Szczepaniak, and G. Fox, Phys.Rev. **D92**, 074004 (2015), arXiv:1506.01764 [hep-ph].

[35] J. Nys, V. Mathieu, C. Fernández-Ramírez, A. N. Hiller Blin, A. Jackura, M. Mikhasenko, A. Pilloni,

A. P. Szczepaniak, G. Fox, and J. Ryckebusch (JPAC), Phys.Rev. **D95**, 034014 (2017), arXiv:1611.04658 [hep-ph].
[36] V. Mathieu, J. Nys, C. Fernández-Ramírez, A. N. Hiller Blin, A. Jackura, A. Pilloni, A. P. Szczepaniak, and G. Fox (JPAC), Phys.Rev. **D98**, 014041 (2018), arXiv:1806.08414 [hep-ph].
[37] M. Shi, I. V. Danilkin, C. Fernández-Ramírez, V. Mathieu, M. R. Pennington, D. Schott, and A. P. Szczepaniak, Phys.Rev. **D91**, 034007 (2015), arXiv:1411.6237 [hep-ph].
[38] A. Donnachie and P. V. Landshoff, Nucl.Phys. **B231**, 189 (1984).
[39] Y.-s. Oh and T. S. H. Lee, Phys.Rev. **C69**, 025201 (2004), arXiv:nucl-th/0306033 [nucl-th].
[40] G. Girardi, C. Godreche, and H. Navelet, Nucl.Phys. **B76**, 541 (1974).
[41] A. C. Irving and R. P. Worden, Phys.Rept. **34**, 117 (1977).
[42] J. Nys, A. Hiller Blin, V. Mathieu, C. Fernández-Ramírez, A. Jackura, A. Pilloni, J. Ryckebusch, A. Szczepaniak, and G. Fox (JPAC), Phys.Rev. **D98**, 034020 (2018), arXiv:1806.01891 [hep-ph].
[43] F. James and M. Roos, Comput.Phys.Commun. **10**, 343 (1975).
[44] S. D. Bass and P. Moskal, Rev.Mod.Phys. **91**, 015003 (2019), arXiv:1810.12290 [hep-ph].
[45] E. Barrelet, Nuovo Cim. **A8**, 331 (1972).
[46] B. Efron and R. Tibshirani, *An Introduction to the Bootstrap*, Chapman & Hall/CRC Monographs on Statistics & Applied Probability (Taylor & Francis, 1994).
[47] J. Landay, M. Döring, C. Fernández-Ramírez, B. Hu, and R. Molina, Phys.Rev. **C95**, 015203 (2017), arXiv:1610.07547 [nucl-th].
[48] R. Navarro Pérez, J. E. Amaro, and E. Ruiz Arriola, Phys.Lett. **B738**, 155 (2014), arXiv:1407.3937 [nucl-th].